A multifiber Timoshenko beam with embedded discontinuities

Ibrahim Bitar, Nathan Benkemoun, Panagiotis Kotronis, Stéphane Grange

A multifiber Timoshenko beam with embedded discontinuities

Ibrahim Bitar[a,*], Nathan Benkemoun[c], Panagiotis Kotronis[a], Stéphane Grange[b]

[a] *École Centrale de Nantes, Université de Nantes, CNRS, Institut de Recherche en Génie Civil et Mécanique (GeM), UMR 6183, 1 rue de la Noë, BP 92101, 44321 Nantes cedex 3, France*
[b] *Univ. Lyon, INSA-Lyon, SMS-ID, F-69621 Villeurbanne cedex, France*
[c] *IUT Saint-Nazaire, Université de Nantes, CNRS, Institut de Recherche en Génie Civil et Mécanique (GeM), UMR 6183, 58 rue Michel Ange, 44600 Saint-Nazaire, France*

An enhanced high order multifiber Timoshenko beam is introduced to simulate structural behavior up to failure. The beam is displacement based and geometrically linear, its section can be of arbitrary shape and a local constitutive law is assigned to each fiber. The Strong Discontinuity Approach is adopted to enhance the displacement field of the fibers to describe crack openings. The material behaviour at the discontinuity is characterized by a linear cohesive law linking the axial stress and the displacement jump. The variational formulation is presented in the context of the incompatible modes method and details are given on the corresponding computational procedure and the numerical integration of the constitutive laws. The simulation of the non linear behavior of a cantilever beam structure and of a reinforced concrete frame are provided to illustrate the performance of the novel enhanced high order multifiber Timoshenko beam.

1. Introduction

Experimental observations show that under severe static or dynamic loadings strains localize in specific zones sometimes called 'plastic hinges'. With increasing loading, discontinuities can appear leading to partial or total structural collapse. Among the different existing numerical models to study post-peak behavior and failure, beams permit to reduce the necessary number of degrees of freedom and are therefore computational very efficient.

A novel enhanced high order multifiber Timoshenko beam is introduced in this article. The beam is displacement based and geometrically linear, its section can be of arbitrary shape and a local constitutive law is assigned to each fiber. The Strong Discontinuity Approach (SDA) is adopted and the material behaviour at the discontinuity is characterized by a linear cohesive law linking the axial stress and the displacement jump. When a significant amount of fibers reaches failure, failure at the beam and structural level can be therefore 'naturally' reproduced.

Several finite element multifiber beam formulations have been developed and implemented in various Finite Element codes [1–4]. Multifiber beams have proven highly effective for civil engineering applications: non-linear analysis of beams or walls with non-homogeneous sections (e.g. reinforced concrete (RC)) [5–8]; Soil-Structure Interaction problems [9]; Fiber Reinforcing Polymer confinement [10]; seismic vulnerability assessment of retrofitted RC structures [11]; sections submitted to bending, shearing or torsion [12], flexure-shear interaction [13], axial and bending interactions [1–3,14,15]. Euler-Bernoulli multifiber beam formulations are used when the shear effects are negligible [14]. Timosheko formulations are more suitable to reproduce the interactions between axial forces, shear forces and moments [5,12,16–23].

* Corresponding author.
E-mail address: ibrahim.bitar@live.com (I. Bitar).

In order to realistically reproduce strain localization, some authors propose to replace the part of the beam where strain concentration is expected by 3D finite elements. This requires the definition of proper boundary conditions to satisfy compatibility with the adjacent beam elements [24]. An energetic equivalence is therefore considered between the work done at the nodes of the volume interface and the single node of the beam element. Another method, less expensive in terms of calculation time, is to modify the post-peak material behavior at the fiber level [25]. A 3D finite element modelling is first performed to calculate the energy dissipated during the development of the stain localization zone. The energy dissipated by the multifiber model is then considered equal by suitably modifying the constitutive law. This makes possible to derive an estimate of the crack opening in a fiber. A kinematic enhancement of the Timoshenko beam can be also adopted. In [12], the authors proposed to enhance the kinematics of the multifiber section of a Timoshenko beam by a torsional warping function calculated solving of a local problem. [26] propose to update the torsion warping function at each calculation step. A multifiber kinematic enhancement is also introduced in [27] to take into account the effect of transverse reinforcements in reinforced concrete sections.

In order to simulate failure and to describe crack openings with classical (no multifiber) beams, several authors enhanced the kinematic using the Strong Discontinuity Approach (SDA). The material behaviour at the discontinuity is characterized by a generalized law, linking for example the bending moment and the rotational jump, which allows capturing the released fracture energy [28–36]. A generalized higher order Timoshenko beam with embedded rotation discontinuity has been recently presented by the authors of this article in [37].

Up to now however, few authors have tried to combine SDA and multifiber beams. In [38], the authors developed a multifiber Timoshenko beam with a discontinuity of the axial displacement at the fiber level. In [22], the authors presented an enhanced multifiber Timoshenko beam for reinforced concrete structures. The displacement field within the fiber is enhanced by one strong discontinuity variable to describe the local failure. Concrete is modeled by means of a one-dimensional damage model coupled to a cohesive model and steel with a one-dimensional elasto-plastic model coupled to a cohesive model. In the following, the model of [22,38] is referred as Full-Linear-Independent (**FLI**) since linear functions are used to interpolate the displacement fields at the beam level.

We present in this article the way to combine SDA (rotation discontinuity) with a higher order multifiber Timoshenko beam. The original beam formulation has shape functions of order three for the transverse displacements and two for the rotations. It is free of shear locking and one element is able to predict the exact tip displacements for any complex distributed loadings and any suitable boundary conditions [23]. In the following, it is stated as Full-Cubic-Quadratic (**FCQ**) and its performance has been already compared with respect to other beam formulations found in the literature [39–41] in one of the previous articles of the authors [42].

This article is structured as follows: Section 2 presents the enhanced formulation of the **FCQ** multifiber Timoshenko beam and describes the discontinuity kinematics. The variational formulation, the way to obtain the equilibrium equations and specific details on the determination of the enhancement functions are also provided. Section 3 introduces the constitutive laws and Section 4 the computational procedure. Two numerical applications are finally studied in Section 5 to show the performance of the novel enhanced high order multifiber beam.

2. Enhanced multifiber Timoshenko Full-Cubic-Quadratic beam

2.1. Timoshenko FCQ beam

2.1.1. Modified shape functions considering an internal rotational degree of freedom

Fig. 1 illustrates a Timoshenko **FCQ** beam element denoted e (for simplicity reasons, presentation is provided hereafter in 2D). We note L_e the length of the beam, i and j the external nodes and k the internal node.

At time t, the generalized displacements $\mathbf{U}_S$ of a section S located at position x of the beam element axis are:

$$\mathbf{U}_S\begin{pmatrix} x,\ t \end{pmatrix} = \begin{bmatrix} U_x(x,\ t) \\ V_y(x,\ t) \\ \Theta_z(x,\ t) \end{bmatrix} = \begin{bmatrix} \mathbf{N}^u(x)\mathbf{d}_e(t) \\ \mathbf{N}^v(x)\mathbf{d}_e(t) \\ \mathbf{N}^\theta(x)\mathbf{d}_e(t) \end{bmatrix} \tag{1}$$

U_x being the longitudinal displacement, V_y the transverse displacement and Θ_z the rotation of the section S. $\mathbf{d}_e$ is the nodal displacement vector of the **FCQ** formulation defined by:

$$\mathbf{d}_e = [U_{xi}\ \ V_{yi}\ \ \Theta_{zi}\ \ \Delta V^1_{yk}\ \ \Delta\Theta_{zk}\ \ \Delta V^2_{yk}\ \ U_{xj}\ \ V_{yj}\ \ \Theta_{zj}] \tag{2}$$

where ΔV^1_{yk}, $\Delta\Theta_{zk}$ and ΔV^2_{yk} are the degrees of freedom of the internal node (with no specific physical meaning) [23].

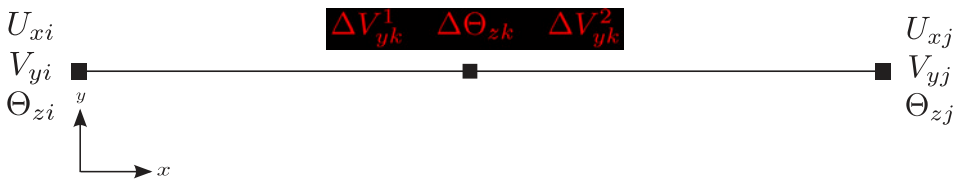

Fig. 1. Timoshenko **FCQ** beam [23].

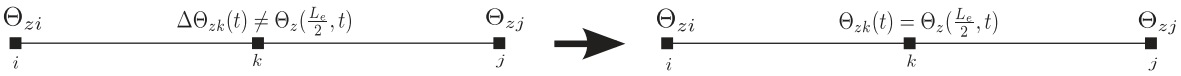

Fig. 2. Modified Timoshenko **FCQ** beam.

$\mathbf{N}^u$, $\mathbf{N}^v$ and $\mathbf{N}^\theta$ are the shape functions of the three displacement components defined as [23]:

$$\begin{bmatrix} \mathbf{N}^u(x) \\ \mathbf{N}^v(x) \\ \mathbf{N}^\theta(x) \end{bmatrix} = \begin{bmatrix} N_1^u & 0 & 0 & 0 & 0 & 0 & N_2^u & 0 & 0 \\ 0 & N_2^v & 0 & N_7^v & 0 & N_9^v & 0 & N_5^v & 0 \\ 0 & 0 & N_3^\theta & 0 & N_8^\theta & 0 & 0 & 0 & N_6^\theta \end{bmatrix}, \tag{3}$$

where

$$\begin{aligned} N_1^u &= 1 - \tfrac{x}{L_e} & N_7^v &= 2\left(1 - \tfrac{x}{L_e}\right)^2\left(\tfrac{x}{L_e}\right) & N_3^\theta &= \left(1 - \tfrac{x}{L_e}\right)\left(1 - 3\tfrac{x}{L_e}\right) \\ N_2^u &= \tfrac{x}{L_e} & N_9^v &= -2\left(\tfrac{x}{L_e}\right)^2\left(1 - \tfrac{x}{L_e}\right) & N_8^\theta &= 1 - \left(1 - 2\tfrac{x}{L_e}\right)^2 \\ N_2^v &= \left(1 - \tfrac{x}{L_e}\right)^2\left(1 + 2\tfrac{x}{L_e}\right) & N_5^v &= \left(\tfrac{x}{L_e}\right)^2\left(3 - 2\tfrac{x}{L_e}\right) & N_6^\theta &= -\left(\tfrac{x}{L_e}\right)\left(2 - 3\tfrac{x}{L_e}\right) \end{aligned} \tag{4}$$

With respect to the original formulation [23], a slight modification is introduced hereafter re-writing the interpolation of the rotations as a function of the rotations at the nodes i and j and the rotation at the note k situated at the middle of the element $\Theta_{zk} = \Theta_z(\frac{L_e}{2}, t)$ (see Fig. 2). To do this, the relation between $\Delta\Theta_{zk}$ and Θ_{zk} is first found calculating the rotation at the middle of the element from Eq. (1) (expressing the shape functions N_3^θ, N_8^θ and N_6^θ at $x = \frac{L_e}{2}$):

$$\Theta_z\left(\frac{L_e}{2}, t\right) = \Theta_{zk}(t) = \Delta\Theta_{zk}(t) - \frac{1}{4}[\Theta_{zi}(t) + \Theta_{zj}(t)] \tag{5}$$

Therefore,

$$\Delta\Theta_{zk}(t) = \Theta_{zk}(t) + \frac{1}{4}[\Theta_{zi}(t) + \Theta_{zj}(t)] \tag{6}$$

Introducing Eq. (6) in Eq. (1), the rotation field can now be interpolated function of the rotations at the external notes i, j and the rotation at the middle point k:

$$\Theta_z\left(x, t\right) = \sum_{\alpha=i,j,k} N_\alpha^{\theta^*}(x)\Theta_{z\alpha}(t) = \mathbf{N}^{\theta^*}(x)\mathbf{d}_e(t) \tag{7}$$

with the three modified interpolation functions:

$$\begin{aligned} N_3^{\theta^*}(x) &= N_3^\theta(x) + \tfrac{1}{4}N_8^\theta(x) = 1 - \tfrac{3x}{L_e} + \tfrac{2x^2}{L_e^2} \\ N_6^{\theta^*}(x) &= N_6^\theta(x) + \tfrac{1}{4}N_8^\theta(x) = -\tfrac{x}{L_e} + \tfrac{2x^2}{L_e^2} \\ N_8^{\theta^*}(x) &= N_8^\theta(x) = \tfrac{4x}{L_e} - \tfrac{4x^2}{L_e^2} \end{aligned} \tag{8}$$

Eq. (8) satisfy all the necessary properties of a shape function [37,43,44]. The above modification helps to determine the enhancement functions of the multifiber Timoshenko **FCQ** beam element (see Section 2.3) and has no influence on the performance of the **FCQ** formulation [23,42].

The use of linear interpolation functions for the axial displacement and quadratic approximation for the rotation provides inconsistent results when N-M interactions and nonlinear material effects are considered. A solution to this problem was provided by the authors in [42] using higher order interpolation functions for the axial displacement field for the **FCQ** beam. In this paper however we focus on M-T interactions and therefore the initial version of the formulation is adopted [23].

2.1.2. Axial displacement: fiber vs. beam axis interpolation

Following the planar section hypothesis (Timoshenko theory), the displacements of a fiber of coordinates x, y at instant t are deduced from the generalised displacements (Eq. (1)) as:

$$\begin{aligned} u_x(x, y, t) &= U_x(x, t) - y\Theta_z(x, t) \\ v_y(x, y, t) &= V_y(x, t) \end{aligned} \tag{9}$$

The multifiber beam formulation can be presented in two equivalent: an interpolation at the fiber level (Path a) and an interpolation at the beam level axis (Path b), illustrated in Fig. 3 and Eq. (10).

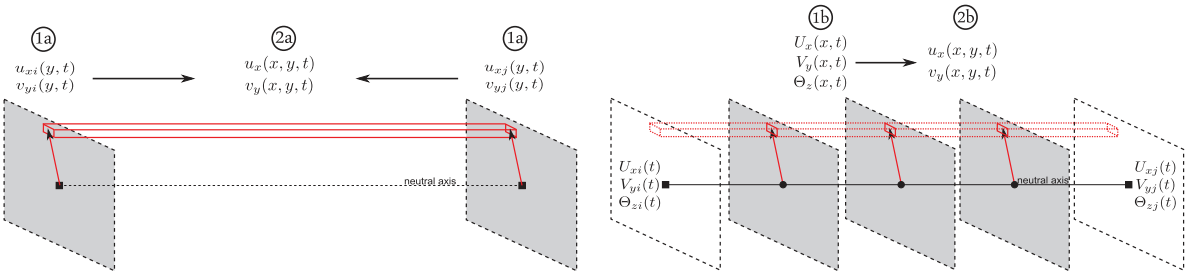

(a) Path a (b) Path b

Fig. 3. Two multifiber beam formulations: (a) fiber level (Path a), (b) beam level axis (Path b).

$$
\begin{aligned}
&\text{a}\Rightarrow \begin{Bmatrix} U_{xi}(t)\\ V_{yi}(t)\\ \Theta_{zi}(t)\\ U_{xj}(t)\\ V_{yj}(t)\\ \Theta_{zj}(t)\end{Bmatrix} \overset{1a}{\Rightarrow} \begin{Bmatrix} u_{xi}(y,t)\\ v_{yi}(y,t)\\ u_{xj}(y,t)\\ v_{yj}(y,t)\end{Bmatrix} \overset{2a}{\searrow}\\
&\qquad\qquad \Rightarrow \begin{matrix} u_x(x,y,t)\\ v_y(x,y,t)\end{matrix} \overset{3}{\Rightarrow} \begin{matrix} \varepsilon_x(x,y,t)\\ \gamma_{xy}(x,y,t)\end{matrix} \overset{4}{\Rightarrow} \begin{matrix} \sigma_x(x,y,t)\\ \tau_{xy}(x,y,t)\end{matrix} \overset{5}{\Rightarrow} \begin{matrix} F_{fiber}(y)\\ K_{fiber}(y)\end{matrix} \overset{6}{\Rightarrow} \begin{matrix} F_e\\ K_e\end{matrix}\\
&b\Rightarrow \begin{Bmatrix} U_{xi}(t)\\ V_{yi}(t)\\ \Theta_{zi}(t)\\ U_{xj}(t)\\ V_{yj}(t)\\ \Theta_{zj}(t)\end{Bmatrix} \overset{1b}{\Rightarrow} \begin{Bmatrix} U_x(x,t)\\ V_y(x,t)\\ \Theta_z(x,t)\end{Bmatrix} \overset{2b}{\nearrow}
\end{aligned}
\tag{10}
$$

The first formulation, Path (a) in Fig. 3a, consists in calculating the axial displacements vector $\mathbf{d}_f(y,\,t)$ at the nodes of each fiber f of ordinate y considering the hypothesis of planar sections (9). That works:

$$
\mathbf{d}_f\begin{pmatrix} \\ y,\,t\end{pmatrix} = \begin{bmatrix} u_{xi}(y,\,t)\\ u_{xj}(y,\,t)\\ u_{xk}(y,\,t)\end{bmatrix} = \begin{bmatrix} U_{xi}(t) - y\Theta_{zi}(t)\\ U_{xj}(t) - y\Theta_{zj}(t)\\ \frac{U_{xi}(t)+U_{xj}(t)}{2} - y\Theta_{zk}(t)\end{bmatrix}
\tag{11}
$$

Hence, the fiber can be considered as a 1D three-node bar as shown in Fig. 4.

The axial displacement field $u_x(x,\,y,\,t)$ along the fiber is thus interpolated by shape functions $\mathbf{N}_f(x)$ such that:

$$
u_x(x,\,y,\,t) = \mathbf{N}^u(x)\mathbf{d}_e(t) - y\mathbf{N}^{\theta^*}(x)\mathbf{d}_e(t) = \mathbf{N}_f(x)\mathbf{d}_f(y,\,t)
\tag{12}
$$

with

$$
\mathbf{N}_f(x) = [N_{fi}(x)\quad N_{fj}(x)\quad N_{fk}(x)]
\tag{13}
$$

These functions take the same expressions as $N_\alpha^{\theta^*}(x)$ in (8):

$$
N_{fi}(x) = 1 - \frac{3x}{L_e} + \frac{2x^2}{L_e^2},\quad N_{fj}(x) = -\frac{x}{L_e} + \frac{2x^2}{L_e^2},\quad N_{fk}(x) = \frac{4x}{L_e} - \frac{4x^2}{L_e^2}
\tag{14}
$$

As a result, the multifiber beam element formulation is transformed into a combination of 1D three-node bar elements.

On the other hand, Path (b) consists in interpolating the generalized displacement fields with the shape functions of the adopted beam formulation. Then, the axial displacement along each fiber is determined using the planar section hypothesis, Eq. (9), at the integration points. The displacement field is therefore no longer interpolated along each fiber but along the axis of the beam element as follows:

$$
u_x(x,\,y,\,t) = \mathbf{N}^u(x)\mathbf{d}_e(t) - y\mathbf{N}^{\theta^*}(x)\mathbf{d}_e(t) = (\mathbf{N}^u(x) - y\mathbf{N}^{\theta^*}(x))\mathbf{d}_e(t)
\tag{15}
$$

As shown in Sections 2.2, 2.3 and 4 Path (a), Eq. (12), allows writing the axial displacement at the fiber level and thus to define

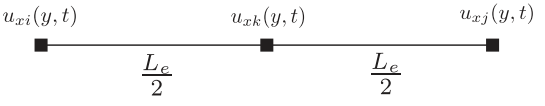

Fig. 4. A three-node fiber.

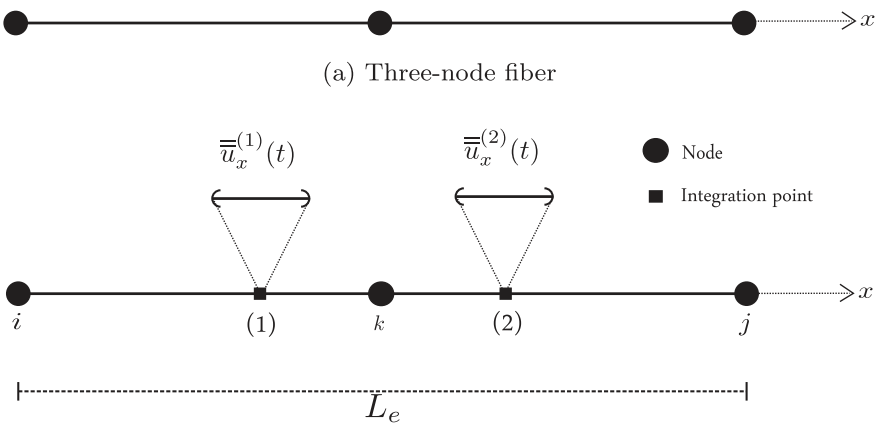

(b) Three-node fiber: two integration points, one discontinuity by integration point.

Fig. 5. (a) Three-node fiber. (b) Three-node fiber: two integration points, one discontinuity by integration point.

the discontinuity kinematics and the corresponding enhancement functions. Path (b), Eq. (15), facilitates the writing of the variational formulation, the numerical implementation procedure and the construction of the element stiffness matrix.

2.2. Fiber kinematic enhancement

We propose hereafter a way to adapt the SDA for beams (see [22,28–34,37,38]) for the higher order multifiber Timoshenko beam introduced in [23].

2.2.1. Enhanced axial displacement

In order to account for several discontinuities within a fiber, the enhanced axial displacement field at the fiber level is written as follows (see Eq. (12)):

$$u_x\left(x,\, y,\, t\right) = \mathbf{N}_f(x)\mathbf{d}_f\left(y,\, t\right) + \sum_{d=1}^{npg} \left([H_{x_d}(x) - \phi^{(d)}(x)]\,\overline{\overline{u}}_x^{(d)}(t)\right) \tag{16}$$

with *npg* the number of integration points, $H_{x_d}(x)$ the Heaviside function, $\phi^{(d)}(x)$ the functions associated with each discontinuity (d) allowing to fulfill the compatibility conditions between the elements and $\overline{\overline{u}}_x^{(d)}(t)$, the displacement discontinuities variables.

Two Gauss integration points are sufficient to obtain an accurate integration of the axial forces at the fiber level since the interpolation functions of the strain field are linear. It is assumed that each integration point carries only one discontinuity (Fig. 5):

The coordinates of the integrations points and the associated integration weights in the real and reference element are:

$$\underbrace{x_{pg}\Big|_{ref} = \left[-\tfrac{1}{\sqrt{3}} \quad \tfrac{1}{\sqrt{3}}\right]}_{\text{Reference element}} \quad \Rightarrow \quad \underbrace{x_{pg}\Big|_{ele} = \left[\left(1 - \tfrac{1}{\sqrt{3}}\right)\tfrac{L_e}{2} \quad \left(1 + \tfrac{1}{\sqrt{3}}\right)\tfrac{L_e}{2}\right]}_{\text{Real element}} \tag{17}$$

$$w_{pg} = [1 \;\; 1] \tag{18}$$

In the proposed model in this paper, each fiber can carry one or two discontinuities. Also, it is a question of enhancing the integration point here rather than enhancing the element. This choice is made in order to respect the ultimate values of the stresses throughout the fiber, especially at the points that interest the calculation, i. e. at the integration points. More details will be addressed when elaborating the equilibrium equations.

2.2.2. Enhanced axial strain

The strain field at the fiber is easily derived from the axial displacement field as follows:

$$\varepsilon_x\left(x,\, y,\, t\right) = \frac{\partial}{\partial x}\{\mathbf{N}_f(x)\mathbf{d}_f(y,\, t)\} + \sum_{d=1}^{npg}\left(\frac{\partial}{\partial x}\{-\phi^{(d)}(x)\}\overline{\overline{u}}_x^{(d)}(t) + \frac{\partial}{\partial x}\{H_{x_d}(x)\}\overline{\overline{u}}_x^{(d)}(t)\right) \tag{19}$$

To simplify the equations, the vector $\overline{\overline{\mathbf{u}}}_x(t)$carrying the discontinuities by fiber is introduced (see Fig. 5):

$$\overline{\overline{\mathbf{u}}}_x(t) = \begin{bmatrix} \overline{\overline{u}}_x^{(1)}(t) \\ \overline{\overline{u}}_x^{(2)}(t) \end{bmatrix} \tag{20}$$

We also use the vector:

$$\mathbf{G}_r(x) = \overline{\mathbf{G}}_r(x) + \overline{\overline{\mathbf{G}}}_r(x) = \overline{\mathbf{G}}_r(x) + \boldsymbol{\delta}_{x_d} \tag{21}$$

divided into a regular (symbol $\bar{\cdot}$) and a singular part (symbol $\bar{\bar{\cdot}}$) where $\overline{\mathbf{G}}_r(x)$ is the vector of the enhancement functions associated with each discontinuity:

$$\overline{\mathbf{G}}_r(x) = [\overline{G}_r^{(1)}(x) \quad \overline{G}_r^{(2)}(x)] \tag{22}$$

with

$$\overline{G}_r^{(d)}(x) = -\frac{\partial}{\partial x}\{\phi^{(d)}(x)\} \qquad d = 1, 2 \tag{23}$$

and $\boldsymbol{\delta}_{x_d}$ the following Dirac functions vector:

$$\boldsymbol{\delta}_{x_d} = [\delta_{x_d}^{(1)}(x) \quad \delta_{x_d}^{(2)}(x)] \tag{24}$$

The index r indicates that the interpolated discontinuities are real variables (see Section 2.3 for the virtual variables). Therefore, the enhanced strain filed takes the following form:

$$\varepsilon_x\left(x, y, t\right) = \underbrace{\mathbf{B}_f(x)\mathbf{d}_f(y, t) + \overline{\mathbf{G}}_r(x)\overline{\overline{\mathbf{u}}}_x(t)}_{\widetilde{\varepsilon}_x(x,y,t)} + \underbrace{\boldsymbol{\delta}_{x_d}\overline{\overline{\mathbf{u}}}_x(t)}_{\overline{\overline{\varepsilon}}_x(x,y,t)} \tag{25}$$

with

$$\mathbf{B}_f(x) = \frac{\partial}{\partial x}\mathbf{N}_f(x) = [B_{fi}(x) \quad B_{fj}(x) \quad B_{fk}(x)] = \left[-\tfrac{3}{L_e} + \tfrac{4x}{L_e^2} \quad -\tfrac{1}{L_e} + \tfrac{4x}{L_e^2} \quad \tfrac{4}{L_e} - \tfrac{8x}{L_e^2}\right] \tag{26}$$

In order to determine the enhancement functions $\overline{G}_r^{(d)}$, known as the compatibility operators, two requirements should be met: (1) the introduction of displacement field discontinuities must not influence the nodal displacements so that the elements compatibility is satisfied. (2) to avoid stress locking phenomena $\overline{G}_r^{(d)}$ must be able to reproduce the zero hinge mode [29]; i.e. in the case of a fully opened discontinuity the cohesive stress at the discontinuity must vanish and the strain $\widetilde{\varepsilon}_x$ must tend to zero.

1st requirement: compatibility

The following three equations have to satisfied:

$$u_x\left(0, y, t\right) = u_i \Rightarrow \sum_{d=1}^{npg}\left([H_{x_d}(0) - \phi^{(d)}(0)]\overline{\overline{u}}_x^{(d)}(t)\right) = 0 \Rightarrow \sum_{d=1}^{npg}\left([0 - \phi^{(d)}(0)]\overline{\overline{u}}_x^{(d)}(t)\right) = 0$$
$$\text{therefore} \quad \forall\, d \in [1, 2] \quad \phi^{(d)}(0) = 0 \tag{27}$$

$$u_x\left(L_e, y, t\right) = u_j \Rightarrow \sum_{d=1}^{npg}\left([H_{x_d}(L_e) - \phi^{(d)}(L_e)]\overline{\overline{u}}_x^{(d)}(t)\right) = 0 \Rightarrow \sum_{d=1}^{npg}\left([1 - \phi^{(d)}(L_e)]\overline{\overline{u}}_x^{(d)}(t)\right) = 0$$
$$\text{therefore} \quad \forall\, d \in [1, 2] \quad \phi^{(d)}(L_e) = 1 \tag{28}$$

$$u_x\left(\tfrac{L_e}{2}, y, t\right) = u_k \Rightarrow \sum_{d=1}^{npg}\left(\left[H_{x_d}(\tfrac{L_e}{2}) - \phi^{(d)}(\tfrac{L_e}{2})\right]\overline{\overline{u}}_x^{(d)}(t)\right) = 0 \Rightarrow \begin{matrix} \sum_{d=1}^{npg}\left(\left[1 - \phi^{(d)}(\frac{L_e}{2})\right]\overline{\overline{u}}_x^{(d)}(t)\right) = 0 \text{ if } x_d = x_1 \\ \sum_{d=1}^{npg}\left(\left[0 - \phi^{(d)}(\frac{L_e}{2})\right]\overline{\overline{u}}_x^{(d)}(t)\right) = 0 \text{ if } x_d = x_2 \end{matrix}$$
$$\text{therefore for } x_1, \quad \phi^{(d)}(\tfrac{L_e}{2}) = 1 \quad \text{and for } x_2, \quad \phi^{(d)}(\tfrac{L_e}{2}) = 0 \tag{29}$$

Following (27)–(29), the enhancement functions $\phi^{(d)}(x)$ corresponding to the two discontinuities can be defined as:

$$\begin{aligned} \phi^{(1)}(x) &= N_{fj}(x) + N_{fk}(x) \quad \text{since} \quad x_1 < \tfrac{L_e}{2} \\ \phi^{(2)}(x) &= N_{fj}(x) \quad \text{since} \quad x_2 > \tfrac{L_e}{2} \end{aligned} \tag{30}$$

The derivatives of these functions give:

$$\begin{aligned} \overline{G}_r^{(1)}(x) &= -(B_{fj}(x) + B_{fk}(x)) = \tfrac{4x}{L_e^2} - \tfrac{3}{L_e} \\ \overline{G}_r^{(2)}(x) &= -B_{fj}(x) = -\tfrac{4x}{L_e^2}x + \tfrac{1}{L_e} \end{aligned} \tag{31}$$

The values of Eq. (31) at the two integration points are summarized in the table below:

Table 1
Values of the kinematic operator $\overline{\mathbf{G}}_r(x)$ at the two integration points.

	x_1	x_2
$\overline{G}_r^{(1)}(x)$	$-\frac{L_e}{2}\left(-1-\frac{2}{\sqrt{3}}\right)$	$\frac{L_e}{2}\left(-1+\frac{2}{\sqrt{3}}\right)$
$\overline{G}_r^{(2)}(x)$	$\frac{L_e}{2}\left(-1+\frac{2}{\sqrt{3}}\right)$	$\frac{L_e}{2}\left(-1-\frac{2}{\sqrt{3}}\right)$

In Table 1, the values of $\overline{G}_r^{(1)}(x_2)$ and $\overline{G}_r^{(2)}(x_1)$ are not zero, indicating that the strain states at the integration points are coupled, i.e. the presence of a discontinuity at the first integration point influences the state of the discontinuity at the second integration point. This leads to a complex numerical implementation, see Section 4.

2nd requirement: zero hinge mode

Eq. (31) should verify the zero hinge mode requirement. Three cases have to be checked: (i) only the first discontinuity is active, (ii) only the second discontinuity is active, (iii) both discontinuities are active.

The first case implies: $\overline{\overline{u}}_x^{(1)} = u_{xk} - u_{xi}$ and $u_{xj} = u_{xk}$. Therefore,

$$\widetilde{\varepsilon}_x\left(x,\,t\right) = \mathbf{B}_f(x)\mathbf{d}_f\left(y,\,t\right) + \overline{G}_r^{(1)}(x)\overline{\overline{u}}_x^{(1)}(t) = B_{fi}(x)u_{xi} + B_{fj}(x)u_{xj} + B_{xk}(x)u_{xk} - \left(B_{fj}(x) + B_{fk}(x)\right)\left(u_{xj} - u_{xi}\right)$$
$$= \underbrace{\left(B_{fi}(x) + B_{fj}(x) + B_{fk}(x)\right)}_{=0}u_{xi} = 0 \tag{32}$$

The second case implies: $\overline{\overline{u}}_x^{(2)} = u_{xj} - u_{xk}$ and $u_{xk} = u_{xi}$. Therefore,

$$\widetilde{\varepsilon}_x\left(x,\,t\right) = \mathbf{B}_f(x)\mathbf{d}_f\left(y,\,t\right) + \overline{G}_r^{(2)}(x)\overline{\overline{u}}_x^{(2)}(t) = B_{fi}(x)u_{xi} + B_{fj}(x)u_{xj} + B_{xk}(x)u_{xk} - B_{fj}(x)\left(u_{xj} - u_{xk}\right) = \underbrace{\left(B_{fi}(x) + B_{fj}(x) + B_{fk}(x)\right)}_{=0}u_{xi}$$
$$= 0 \tag{33}$$

The third case implies: $\overline{\overline{u}}_x^{(2)} = u_{xj} - u_{xk}$ and $\overline{\overline{u}}_x^{(1)} = u_{xk} - u_{xi}$. Therefore,

$$\widetilde{\varepsilon}_x\left(x,\,t\right) = \mathbf{B}_f(x)\mathbf{d}_f\left(y,\,t\right) + \overline{G}_r^{(1)}(x)\overline{\overline{u}}_x^{(1)}(t) + \overline{G}_r^{(2)}(x)\overline{\overline{u}}_x^{(2)}(t) = B_{fi}(x)u_{xi} + B_{fj}(x)u_{xj} + B_{xk}(x)u_{xk} - \left(B_{fj}(x) + B_{fk}(x)\right)\left(u_{xk} - u_{xi}\right)$$
$$- B_{fj}(x)\left(u_{xj} - u_{xk}\right) = \underbrace{\left(B_{fi}(x) + B_{fj}(x) + B_{fk}(x)\right)}_{=0}u_{xi} = 0 \tag{34}$$

Eqs. (32)–(34) show that the compatibility operators $\overline{G}_r^{(d)}$ satisfy the zero hinge mode requirement.

2.3. Variational formulation

2.3.1. Interpolation of the virtual fields

The upscript $\bullet^*$ is adopted hereafter for the virtual variables. The virtual displacements are interpolated with the same shape functions as the real displacements. Using (15), the axial virtual strains take the following expression:

$$\varepsilon_x^*(x,\,y,\,t) = \mathbf{B}_f(x,\,y)\mathbf{d}_e^*(t) + \mathbf{G}_v(x)\overline{\overline{\mathbf{u}}}_x^*(t) \tag{35}$$

where $\mathbf{G}_v$ is the enhancement function of the virtual discontinuities $\overline{\overline{\mathbf{u}}}_x^*$, also known as the equilibrium operator, defined as the sum of a regular $\overline{\mathbf{G}}_v$ and a singular $\overline{\overline{\mathbf{G}}}_v$ part:

$$\mathbf{G}_v(x) = \overline{\mathbf{G}}_v(x) + \overline{\overline{\mathbf{G}}}_v(x) = \overline{\mathbf{G}}_v(x) + \boldsymbol{\delta}_{x_d}(x) \tag{36}$$

The use of (15) enables to write the variational formulation using the virtual values of the nodal degrees of freedom $\mathbf{d}_e^*(t)$, thus facilitating the numerical developments (see Section 4).

The enhancement functions $\overline{G}_v$ associated with virtual discontinuities are not necessarily equal to $\overline{G}_r$ associated with the real discontinuities (see for example [37]). Actually, real discontinuities are interpolated following kinematic considerations (see Section 2.2) while virtual discontinuities are interpolated following static considerations (see Section 2.4). This is in order to satisfy the balance between the discontinuous and the continuous parts in the fiber, as well as the Patch test. Both interpolations in the same formulation are first proposed in [45,46].

Following Timoshenko's theory, the virtual shear strain is constant and calculated as:

$$\gamma_{xy}^{*}\left(x,\,y,\,t\right)=\gamma_{xy}^{*}\left(x,\,t\right)=\frac{\partial}{\partial x}V_{y}^{*}(x)-\Theta_{z}^{*}(x)=\frac{\partial}{\partial x}\mathbf{N}^{v}(x)\mathbf{d}_{e}^{*}(t)-\mathbf{N}^{\Theta}\mathbf{d}_{e}^{*}(t)=\mathbf{B}^{\gamma}(x)\mathbf{d}_{e}^{*}(t) \tag{37}$$

2.3.2. Principle of virtual work

2.3.2.1. Fiber level. The internal work of each fiber is:

$$W_{int}^{f}\left(y,\,t\right)=\int_{\Omega^{f}}\delta\varepsilon_{x}^{*}(x,\,y,\,t)^{T}\sigma_{x}\left(x,\,y,\,t\right)+\delta\gamma_{xy}^{*}(x,\,y,\,t)^{T}\tau_{xy}\left(x,\,y,\,t\right)d\Omega^{f} \tag{38}$$

where σ_x and τ_{xy} are the axial and shear stresses at the fiber, $\delta\varepsilon_x^*$ and $\delta\gamma_{xy}^*$ are respectively the axial and the shear virtual strains variations and Ω^f is the fiber volume.

Introducing (35) and (37) in (38) results:

$$W_{int}^{f}(y,\,t)=\delta\mathbf{d}^{*}(t)^{T}\mathbf{F}_{int,B}^{f}(y,\,t)+\delta\overline{\mathbf{u}}_{x}^{*}(y,\,t)^{T}\mathbf{F}_{int,G}^{f}(y,\,t) \tag{39}$$

where

$$\mathbf{F}_{int,B}^{f}\left(y,\,t\right)=\int_{\Omega^{f}}\left[\mathbf{B}_{f}(x,\,y)\quad\mathbf{B}^{\gamma}(x)\right]^{T}\begin{bmatrix}\sigma_{x}(x,\,y,\,t)\\ \tau_{xy}(x,\,y,\,t)\end{bmatrix}d\Omega^{f} \tag{40}$$

and

$$\mathbf{F}_{int,G}^{f}\left(y,\,t\right)=\int_{\Omega^{f}}\mathbf{G}_{v}(x)^{T}\sigma_{x}\left(x,\,y,\,t\right)d\Omega^{f} \tag{41}$$

Beam level

The internal work at the multifiber beam element level is found simply by summing up the internal work of the fibers:

$$W_{int}^{e}(t)=\sum_{f}^{nfib}W_{int}^{f}\left(y,\,t\right)=\delta\mathbf{d}^{*}(t)^{T}\mathbf{F}_{int,B}^{e}(t)+\sum_{f}^{\overline{n}_{f}}\delta\overline{\mathbf{u}}_{x}^{*}(y,\,t)^{T}\mathbf{F}_{int,G}^{f}\left(y,\,t\right) \tag{42}$$

with $\overline{n}_f$ the number of cracked fibers per beam element. A cracked fiber is a fiber with at least one discontinuity.

Structural level

Finally, the total internal work a the level of the structure is:

$$W_{int}^{str}(t)=\sum_{e}^{nele}W_{int}^{e}(t)=\delta\mathbf{d}^{*}(t)^{strT}\mathbf{F}_{int,B}^{str}(t)+\sum_{e}^{\overline{n}}\sum_{f}^{\overline{n}_{f}}\delta\overline{\mathbf{u}}_{x}^{*}(y,\,t)^{T}\mathbf{F}_{int,G}^{f}\left(y,\,t\right) \tag{43}$$

with $\overline{n}$ the number of elements with at least one cracked fiber.

The introduction of the last expression in the principle of virtual work gives:

$$\begin{aligned}&W_{int}^{str}(t)-W_{ext}^{str}(t)=0\\ &\delta\mathbf{d}^{*}(t)^{strT}(\mathbf{F}_{int,B}^{str}(t)-\mathbf{F}_{ext}^{str}(t))+\sum_{e}^{\overline{n}}\sum_{f}^{\overline{n}_{f}}\delta\overline{\mathbf{u}}_{x}^{*}(y,\,t)^{T}\mathbf{F}_{int,G}^{f}\left(y,\,t\right)=0\end{aligned} \tag{44}$$

The equilibrium of the structure must be respected for all virtual displacements $\delta\mathbf{d}_{str}^{*}(t)$ as well as for any virtual displacement jump $\delta\overline{\mathbf{u}}_{x}^{*}(y,\,t)$ at the fiber level. This provides the following system of equations:

$$\begin{aligned}&\mathbf{F}_{int,B}^{str}(t)-\mathbf{F}_{ext}^{str}(t)=0\\ &\forall\,e\in\{1,\,2,...,\overline{n}\}\ \text{et}\quad\forall\,f\in\{1,\,2,...,\overline{n}_{f}(e)\}:\quad\mathbf{F}_{int,G}^{f}(y,\,t)=0\end{aligned} \tag{45}$$

The first equation corresponds to the overall equilibrium of the structure. The other equations represent the local equilibrium at the level of each fiber with active discontinuities and can be solved locally at the fiber level.

$\mathbf{F}_{int,G}^{f}(y,\,t)$ can be further developed using the decomposition (36) to give:

$$\begin{aligned}\mathbf{F}_{int,G}^{f}(t)\left(y,\,t\right)&=\int_{\Omega^{f}}\mathbf{G}_{v}(x)^{T}\sigma\left(x,\,y,\,t\right)d\Omega^{f}=\int_{\Omega^{f}}\left(\overline{\mathbf{G}}_{v}(x)^{T}+\delta_{x_d}(x)^{T}\right)\sigma\left(x,\,y,\,t\right)d\Omega^{f}=\int_{\Omega^{f}}\overline{\mathbf{G}}_{v}(x)^{T}\sigma\left(x,\,y,\,t\right)d\Omega^{f}+\boldsymbol{\sigma}\left(x_{d},\,y,\,t\right)\\ &=0\end{aligned} \tag{46}$$

with

$$\int_{\Omega^{f}}\boldsymbol{\delta}_{x_d}(x)^{T}\sigma\left(x,\,y,\,t\right)d\Omega^{f}=\boldsymbol{\sigma}\left(x_{d},\,y,\,t\right)$$

leading to:

$$\int_{\Omega^f} \overline{\mathbf{G}}_v(x)^T \sigma\left(x,\, y,\, t\right) d\Omega^f = -\boldsymbol{\sigma}\left(x_d,\, y,\, t\right) = -\mathbf{C}^f\left(y,\, t\right) \tag{47}$$

with $\mathbf{C}^f(y,\, t)$ the vector of cohesive stresses at discontinuities level belonging to the same fiber defined as:

$$\mathbf{C}^f\left(y,\, t\right) = \begin{bmatrix} C^{f,(1)}(y,\, t) \\ C^{f,(2)}(y,\, t) \end{bmatrix} \tag{48}$$

2.4. Determination of $\overline{\mathbf{G}}_v(x)$

It remains to determine the functions $\overline{\mathbf{G}}_v(x) = [\overline{G}_v^{(1)}(x) \quad \overline{G}_v^{(2)}(x)]$. Let's assume a linear function for $\overline{G}_v^{(d)}(x)$ of the form $ax + b$ (a and b constants) and a linear expression for the fiber stress $\sigma(x) = \alpha x + \beta$ (α and β constants). a and b are determined by an identification procedure that ensures the following equality $\int_{\Omega^f} \overline{G}_v^{(d)}(x)^T \sigma(x,\, y,\, t) d\Omega^f = -\sigma(x_d,\, y,\, t)$ (47) for each discontinuity level $x = x_d$. Indeed,

$$\int_{\Omega^f} \left(ax + b\right)\left(\alpha x + \beta\right) d\Omega^f = -\left(\alpha x_d + \beta\right) \quad \underset{\text{with respect to } \alpha \text{ and } \beta}{\overset{\textit{identification}}{\Rightarrow}} \quad \begin{cases} a = \frac{6}{L^2} - \frac{12}{L^3} x_d \\ b = -\frac{4}{L} + \frac{6}{L^2} x_d \end{cases} \tag{49}$$

Therefore, the function $\overline{G}_v^{(d)}(x,\, x_d)$ takes the following general form:

$$\overline{G}_v^{(d)}\left(x,\, x_d\right) = \left[\frac{6}{L_e^2} - \frac{12}{L_e^3} x_d\right] x + \frac{6}{L_e^2} x_d - \frac{4}{L_e} \tag{50}$$

Finally, for $x_d = x_{pg}|_{ele}$ (Eq. (17)), the equilibrium operators are:

$$\begin{aligned} &\overline{G}_v^{(1)}(x) = \tfrac{2\sqrt{3}}{L_e^2} x - \tfrac{1}{L_e}\left(1 + \sqrt{3}\right) \quad \text{with} \quad \overline{G}_v^{(1)}(x_1) = -\tfrac{2}{L_e} \quad \text{and} \quad \overline{G}_v^{(1)}(x_2) = 0 \\ &\overline{G}_v^{(2)}(x) = -\tfrac{2\sqrt{3}}{L_e^2} x - \tfrac{1}{L_e}\left(1 - \sqrt{3}\right) \quad \text{with} \quad \overline{G}_v^{(2)}(x_1) = 0 \quad \text{and} \quad \overline{G}_v^{(2)}(x_2) = -\tfrac{2}{L_e} \end{aligned} \tag{51}$$

An additional verification is required to validate the choice of the equilibrium operator $\overline{G}_v^{(d)}(x)$. The enhancement method with embedded discontinuities is similar to the incompatible mode method and as mentioned in the literature [47] the equilibrium operator should verify the Patch test. This test, initially proposed by [48], defines a convergence condition during mesh refinement (the elementary strains and stresses should stay constant). In other words, this test guarantees the ability to represent a constant state of stress per element [49].

The patch test requires that the additional virtual work associated with the enhancement must be zero if the stress is constant along the element. This results the following condition:

$$\int_{L^e} \overline{G}_v^{(d)}(x) dx = -1 \tag{52}$$

This condition is easily verified using Eq. (50).

3. Constitutive laws

In an enhanced multifiber beam, each fiber corresponds to a specific material. Constitutive laws composed of a continuous and a cohesive part should be therefore defined at the fiber level. A damage mechanics law, an elasto-plastic law and the corresponding cohesive laws are detailed hereafter. This choice is particularly suitable for reinforced concrete structures (see Section 5), where damage mechanics is often adopted for concrete and plasticity for steel. The laws are presented in 1D as shear is considered decoupled and linear elastic (see Section 3.3).

3.1. Damage mechanics model – cohesive model

3.1.1. Continuous part

In damage mechanics constitutive laws, damage evolution is often driven by a strain threshold [50–54,10,55]. A stress threshold is however chosen hereafter in order to simplify the numerical implementation. The damage model developed in [49,22] is adopted. The origin of this model goes back to the work of [56]. A scalar internal damage variable called compliance and noted $\overline{D}$ is introduced such that the 1D strain-stress relation takes the following form:

$$\bar{\varepsilon} = \overline{D}\sigma \;\text{ avec }\; \overline{D} \in \left[\frac{1}{E}, \infty\right] \tag{53}$$

The stress-based damage threshold surface becomes:

$$\overline{\phi} = |\sigma| - (\sigma_{by} - \bar{q}) \leqslant 0 \tag{54}$$

where σ_{by} the elastic limit for a material that may have a different behavior in compression and tension (e.g. concrete).

$$\sigma_{by} = \begin{cases} \sigma_{by}^{c} & \text{for compression} \\ \sigma_{by}^{t} & \text{for tension} \end{cases} \tag{55}$$

$\bar{q}$ the stress-like variable associated with the hardening mechanism controling the evolution of the damage threshold surface (50)

$$\bar{q} = -H_b\bar{\xi} \quad \text{with} \quad H_b = \begin{cases} H_b^{c} & \text{for compression} \\ H_b^{t} & \text{for tension} \end{cases} \tag{56}$$

H_b the (positive) damage hardening modulus, $\bar{\xi}$ the strain-like internal variable that controls the hardening mechanism. For more details on the thermodynamic formulation of this model, the reader is referred to the work of [49]. In the following, only those elements necessary for understanding the article are presented.

The free energy $\overline{\Psi}$ is written as follows:

$$\overline{\Psi}\left(\overline{D}, \bar{\xi}\right) = \frac{1}{2}\bar{\varepsilon}\overline{D}^{-1}\bar{\varepsilon} + \frac{1}{2}\bar{\xi}H_b\bar{\xi} \tag{57}$$

The dissipated energy $\overline{D}_b$ due to damage is (where the symbol $\dot{\bullet}$ is the derivative with respect to time):

$$\overline{D}_b = \int_\Omega \sigma\dot{\bar{\varepsilon}} - \dot{\overline{\Psi}}d\Omega = \int_\Omega \frac{1}{2}\sigma\dot{\overline{D}}\sigma + \bar{q}\dot{\bar{\xi}}d\Omega > 0 \tag{58}$$

As usual, the evolution of the internal variables are determined using the principle of maximum dissipation; among all permissible stresses, those that maximize dissipation are selected.

$$\begin{aligned} \dot{\overline{D}} &= \dot{\bar{\gamma}}\frac{1}{\sigma}\frac{\partial\bar{\phi}}{\partial\sigma} = \dot{\bar{\gamma}}\frac{sign(\sigma)}{\sigma} \\ \dot{\bar{\xi}} &= \dot{\bar{\gamma}}\frac{\partial\bar{\phi}}{\partial\bar{q}} = \dot{\bar{\gamma}} \end{aligned} \tag{59}$$

with $\dot{\bar{\gamma}}$ the Lagrange multiplier.

The Kuhn-Tucker conditions and the consistency condition are:

$$\dot{\bar{\gamma}} \geqslant 0 \quad \bar{\phi} \leqslant 0 \quad \dot{\bar{\gamma}}\bar{\phi} = 0 \quad \dot{\bar{\gamma}}\dot{\bar{\phi}} = 0$$

The damage process is active when $\dot{\bar{\gamma}}$ is positive. Therefore, the value of $\dot{\bar{\phi}}$ must necessarily be zero to comply with the consistency condition. This makes possible to deduce the expression of $\dot{\bar{\gamma}}$:

$$\dot{\bar{\gamma}} = \frac{sign(\sigma)\,\overline{D}^{-1}\,\dot{\bar{\varepsilon}}}{\overline{D}^{-1} + H_b} \tag{60}$$

Finally, the stress rate is written as function of the strain rate:

$$\dot{\sigma} = \begin{cases} \overline{D}^{-1}\dot{\bar{\varepsilon}} & \text{if } \dot{\bar{\gamma}} = 0 \\ \frac{\overline{D}^{-1}H_b}{\overline{D}^{-1}+H_b}\dot{\bar{\varepsilon}} & \text{if } \dot{\bar{\gamma}} > 0 \end{cases} \tag{61}$$

3.1.2. Cohesive part

A cohesive model is adopted to describe the behaviour at each discontinuity. The discontinuity activation criterion is again formulated in terms of stresses; a failure surface $\overline{\phi}^{(d)}$ is introduced at each integration point in order to check the activation and evolution of the discontinuity.

$$\overline{\phi}^{(d)}(t) = |C^{(d)}(t)| - (\sigma_{bu} - \overline{q}^{(d)}(t)) \qquad d = 1, 2 \tag{62}$$

where $C^{(d)}(t)$is the cohesive stress determined by Eq. (47), written as:

$$C^{(d)}(y, t) = \sigma(x_d, y, t) = \sigma(x_{pg}, y, t) \tag{63}$$

Since the discontinuities (d) occur at the integration points (pg), the cohesive stresses $C^{(d)}(y, t)$ should be equal to the continuous stresses $\sigma(x_{pg}, y, t)$. Therefore, the failure surfaces $\overline{\phi}^{(d)}$ at the integration points can be written as:

$$\overline{\phi}^{(pg)}(t) = |\sigma(x_{pg}, y, t)| - (\sigma_{bu} - \overline{q}(x_{pg}, t)) \tag{64}$$

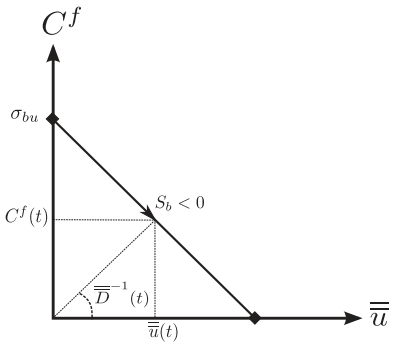

Fig. 6. Cohesive model.

where σ_{bu} is the ultimate stress, that may differ in compression and tension:

$$\sigma_{bu} = \begin{cases} \sigma_{bu}^c & \text{for compression} \\ \sigma_{bu}^t & \text{for tension} \end{cases} \tag{65}$$

$\overline{\overline{q}}$ is the stress-like variable associated with the cohesive model defined as:

$$\overline{\overline{q}}\left(x_{pg},\, t\right) = -S\overline{\overline{\xi}}\left(x_{pg},\, t\right) \quad \text{with} \quad S_b = \begin{cases} S_b^c = -\frac{\sigma_{bu}^{c\,2}}{2G_b^c} & \text{for compression} \\ S_b^t = -\frac{\sigma_{bu}^{t\,2}}{2G_b^t} & \text{for tension} \end{cases} \tag{66}$$

S_b the softening (negative) modulus, G_b^c and G_b^t the compression and tensile failure energies and $\overline{\overline{\xi}}$ the strain-like internal variable whose role is to control softening.

The cohesive behaviour is defined by the following relation:

$$\overline{\overline{u}}\,(x_{pg},\, t) = \overline{\overline{D}}\,(x_{pg},\, t) C^f(x_{pg},\, t) \tag{67}$$

with $\overline{\overline{D}}$ the compliance variable associated with cohesive model. This variable increases progressively with the discontinuity $\overline{\overline{u}}\,(x_{pg},\, t) = \overline{\overline{u}}^{(d)}(t)$. Fig. 6 illustrates the cohesive model.

The relation between the cohesive stress and the discontinuity can be also expressed as:

$$C^f(x_{pg},\, t) = S_b \overline{\overline{u}}\,(x_{pg},\, t) + \sigma_{bu} \tag{68}$$

The total free energy of a fiber with several discontinuities takes the following form:

$$\Psi(t) = \overline{\Psi}(t) + \boldsymbol{\delta}_{x_d} \overline{\boldsymbol{\Psi}}(t) \tag{69}$$

with $\boldsymbol{\delta}_{x_d}$ the Dirac function vector defined in Eq. (24) and $\overline{\boldsymbol{\Psi}}(t)$the free energy vector associated with the discontinuities defined as:

$$\overline{\boldsymbol{\Psi}}(t) = \begin{bmatrix} \overline{\overline{\Psi}}^{(1)}(t) \\ \overline{\overline{\Psi}}^{(2)}(t) \end{bmatrix} \tag{70}$$

where $\overline{\overline{\Psi}}^{(1)}$ and $\overline{\overline{\Psi}}^{(2)}$ are respectively the free energies associated with discontinuities 1 and 2. The expressions are determined according to the corresponding internal variables of the cohesive model:

$$\overline{\overline{\Psi}}^{(d)}(t) = \frac{1}{2}(\overline{\overline{D}}^{(d)})^{-1}(\overline{\overline{u}}^{(d)})^2 + \frac{1}{2} S_b (\overline{\overline{\xi}}^{(d)})^2 \qquad d = 1,\, 2 \tag{71}$$

Using the strain Eq. (25) and the expression of total free energy (69), one can deduce the total dissipation at the fiber level as:

$$D^{tot}(y,\, t) = \overline{D}\,(y,\, t) + \overline{\overline{D}}\,(y,\, t) \tag{72}$$

where $\overline{\overline{D}}$ is the dissipation due to discontinuities:

$$\overline{\overline{D}}\left(y,\, t\right) = \int_{\Omega^f} \left[\sigma\left(x,\, y,\, t\right)\overline{\overline{\varepsilon}}_x - \sum_{d=1}^{2} \dot{\overline{\overline{\Psi}}}^{(d)}\left(y,\, t\right)\right] d\Omega^f = \mathbf{C}^f(y,\, t)^T \overline{\overline{\mathbf{u}}}_x(t) - \boldsymbol{\delta}_x \dot{\overline{\overline{\boldsymbol{\Psi}}}}\left(y,\, t\right) \tag{73}$$

Among the admissible internal variables that verify the failure criteria, those that maximize dissipation are selected. To do this, a Lagrange multiplier denoted $\overline{\overline{y}}$ is introduced. Therefore, the evolution equations of the internal variables are determined as:

$$\begin{aligned}\dot{\overline{D}} &= \dot{\bar{\gamma}}\frac{sign(C^f)}{C^f}\\ \dot{\bar{\xi}} &= \dot{\bar{\gamma}}\\ \dot{\overline{u}} &= \dot{\bar{\gamma}} sign(C^f)\end{aligned} \tag{74}$$

Finally, in order to determine the Lagrange multiplier $\dot{\bar{\gamma}}$ the consistency and Kuhn-Tucker conditions are used:

$$\dot{\bar{\gamma}} \geqslant 0, \quad \overline{\phi} \leqslant 0, \quad \dot{\bar{\gamma}}\,\overline{\phi} = 0, \quad \dot{\bar{\gamma}}\,\dot{\overline{\phi}} = 0 \tag{75}$$

If the softening mechanism is active, the multiplier $\dot{\bar{\gamma}}$ is strictly positive, which means that $\dot{\overline{\phi}}$ must be zero to respect $\dot{\bar{\gamma}}\,\dot{\overline{\phi}} = 0$. Using Eq. (62) and $\dot{\overline{\phi}} = 0$ result to:

$$\dot{\bar{\gamma}} = \frac{1}{S_b}\dot{C}^f sign(C^f) \tag{76}$$

The cohesive force is finally given by:

$$C^f = \begin{cases} \overline{D}^{-1}\overline{u} & \text{pour } \dot{\bar{\gamma}} = 0 \\ (\sigma_{bu} + S_b\bar{\xi})sign(C^f) & \text{pour } \dot{\bar{\gamma}} > 0 \text{ and } \bar{q} < \sigma_{bu} \\ 0 & \text{pour } \dot{\bar{\gamma}} > 0 \text{ and } \bar{q} = \sigma_{bu} \end{cases} \tag{77}$$

More information on the elaboration of these equations can be found in [22,44].

3.2. Elasto-plastic model – cohesive model

3.2.1. Continuous part

A classical 1D elasto-plastic model is briefly presented hereafter (for more details see [57]). As usual, the partition of (regular) strains into an elastic and a plastic component is assumed:

$$\bar{\varepsilon}(x, t) = \bar{\varepsilon}^e(x, t) + \bar{\varepsilon}^p(x, t) \tag{78}$$

The elastic and hardening behaviours are assumed to decoupled and therefore the free energy $\overline{\Psi}$ can be also decoupled into an elastic and a hardening term as follows:

$$\overline{\Psi}\left(\bar{\varepsilon}^e, \bar{\xi}\right) = \frac{1}{2}E_s(\bar{\varepsilon}^e)^2 + \frac{1}{2}H_s(\bar{\xi})^2 \tag{79}$$

with E_s the Young modulus and H_s the hardening modulus. The elastic threshold is expressed as:

$$\overline{\phi} = |\sigma| - (\sigma_{sy} - \bar{q}), \tag{80}$$

with σ_{sy} the elastic limit and $\bar{q}$ the stress-variable hardening variable. $\overline{\phi}$ is always negative when in elasticity. Once the elastic limit σ_{sy} is reached, the material enters the plastic domain. As a result, the internal values associated with plasticity are activated and begin to evolve. The plastic dissipation is written as:

$$\overline{D}^p = \int_\Omega [\sigma^T\dot{\bar{\varepsilon}}^p + \bar{q}\dot{\bar{\xi}}]d\Omega \tag{81}$$

In order to determine the evolution equations of the internal variables, the classical principle of maximum dissipation using the Lagrange multiplier $\bar{\gamma}$ is applied. It is found that:

$$\begin{aligned}\dot{\bar{\varepsilon}}^p &= \dot{\bar{\gamma}}\frac{\partial\overline{\phi}}{\partial\sigma} = sign(\sigma)\dot{\bar{\gamma}}\\ \dot{\bar{\xi}} &= \dot{\bar{\gamma}}\frac{\partial\overline{\phi}}{\partial\bar{q}} = \dot{\bar{\gamma}}\end{aligned} \tag{82}$$

Using the consistency and the Kuhn-Tucker conditions, the rate of the Lagrange multiplier $\dot{\bar{\gamma}}$ is finally found:

$$\dot{\gamma} = \frac{\frac{\partial\overline{\phi}}{\partial\sigma}E_s\dot{\bar{\varepsilon}}}{\frac{\partial\overline{\phi}}{\partial\sigma}E_s\frac{\partial\overline{\phi}}{\partial\sigma} + \frac{\partial\overline{\phi}}{\partial\bar{q}}H_s\frac{\partial\overline{\phi}}{\partial\bar{q}}} \tag{83}$$

3.2.2. Cohesive part

The discontinuity represents a cohesive zone of zero thickness and appears at the integration points $x_d = x_{pg}$ of the fiber when the stress exceeds a critical value σ_u. The failure surface is written in terms of the cohesive force C as follows:

$$\overline{\phi}(C, \overline{U}) = |C| - (\sigma_u + S\overline{u}) \leqslant 0 \tag{84}$$

The total dissipation energy is:

$$D^{tot} = \overline{D} + \overline{\overline{D}} = \int_{\Omega} [\sigma^T \dot{\tilde{\varepsilon}}^p + \overline{q}\dot{\tilde{\xi}}]dx + C^T\dot{\overline{\overline{u}}} \tag{85}$$

As before, an optimization under constraint problem is solved resulting to:

$$\dot{\overline{\overline{u}}} = \dot{\overline{\overline{\gamma}}} sign(C) \tag{86}$$

In order to find the rate of Lagrange multiplier $\dot{\overline{\overline{\gamma}}}$, the Kuhn-Tucker and the consistency conditions are used:

$$\dot{\overline{\overline{\gamma}}} \geqslant 0, \;\; \overline{\overline{\phi}} \leqslant 0, \;\; \dot{\overline{\overline{\gamma}}}\,\overline{\overline{\phi}} = 0, \;\; \dot{\overline{\overline{\gamma}}}\,\dot{\overline{\overline{\phi}}} = 0 \tag{87}$$

It is found that:

$$\dot{\overline{\overline{\gamma}}} = \frac{1}{S}\left|\dot{C}\right| = \frac{1}{S}\dot{C} sign(C) \tag{88}$$

3.3. Shear behaviour

A multifiber Timoshenko beam can also account for the shear behavior. In the following and for simplicity reasons, shear is considered elastic and decoupled from the axial behavior. Therefore,

$$\tau\left(x, y, t\right) = G_c(y)\gamma\left(x, y, t\right) \;\text{ with }\; G_c(y) = \begin{cases} G_{cb} & \text{Shear modulus for the fiber with the 1D damage mechanics law} \\ G_{ca} & \text{Shear modulus for the fiber with the 1D plasticity law} \end{cases} \tag{89}$$

4. Computational procedure

4.1. Linearization of the equilibrium equations

The first step toward the numerical implementation of the higher order enhanced multifiber beam is to linearize the equilibrium Eq. (45). This operation gives the following system:

$$\mathop{\mathrm{A}}_{e=1}^{n_{elm}} \left\{ \begin{bmatrix} \mathbf{K}_{BB} & \mathbf{K}_{BG_1} & \mathbf{K}_{BG_2} & \cdots & \mathbf{K}_{BG_{\overline{n}_f(e)}} \\ \mathbf{K}_{G_1B} & \mathbf{K}_{G_1G_1} & 0 & \cdots & 0 \\ \mathbf{K}_{G_2B} & 0 & \mathbf{K}_{G_2G_2} & \cdots & 0 \\ \cdot & \cdot & \cdot & \cdots & \cdot \\ \cdot & \cdot & \cdot & \cdots & \cdot \\ \mathbf{K}_{G_{\overline{n}_f(e)}B} & 0 & 0 & \cdots & \mathbf{K}_{G_{\overline{n}_f(e)}G_{\overline{n}_f(e)}} \end{bmatrix}_{t+1} \begin{bmatrix} \Delta\mathbf{d}_e \\ \Delta\overline{\overline{\mathbf{u}}}_x(y_1^e, t) \\ \Delta\overline{\overline{\mathbf{u}}}_x(y_2^e, t) \\ \cdot \\ \cdot \\ \Delta\overline{\overline{\mathbf{u}}}_x\left(y^e_{\overline{n}_f(e)}, t\right) \end{bmatrix}_{t+1} = \begin{bmatrix} -\left(\mathbf{F}^e_{int,B} - \mathbf{F}^e_{ext}\right) \\ 0 \\ 0 \\ \cdot \\ \cdot \\ 0 \end{bmatrix}_{t+1} \right\} \tag{90}$$

with

$$\mathbf{K}_{BB}(t) = \sum_{f=1}^{n_f} \mathbf{K}_{BB_f}\left(y, t\right) \tag{91}$$

$$\mathbf{K}_{BB_f}\left(y, t\right) = \int_{\Omega^f} \mathbf{B}^f(x, y)^T \frac{\partial \sigma_x}{\partial \varepsilon_x}\left(x, y, t\right)\mathbf{B}^f\left(x, y\right)d\Omega^f \tag{92}$$

$$\mathbf{K}_{BG_f}\left(y, t\right) = \int_{\Omega^f} \mathbf{B}^f(x, y)^T \frac{\partial \sigma_x}{\partial \widetilde{\varepsilon}_x}\left(x, y, t\right)\overline{\mathbf{G}}_r(x)d\Omega^f \tag{93}$$

$$\mathbf{K}_{G_fB}\left(y, t\right) = \int_{\Omega^f} \overline{\mathbf{G}}_v(x)^T \frac{\partial \sigma_x}{\partial \widetilde{\varepsilon}_x}\left(x, y, t\right)\mathbf{B}^f\left(x, y\right)d\Omega^f \tag{94}$$

$$\mathbf{K}_{G_fG_f}\left(y, t\right) = \int_{\Omega^f} \overline{\mathbf{G}}_v(x)^T \frac{\partial \sigma_x}{\partial \widetilde{\varepsilon}_x}\left(x, y, t\right)\overline{\mathbf{G}}_r(x)d\Omega^f + \frac{\partial \mathbf{C}^f}{\partial \overline{\overline{\mathbf{u}}}_x}A^f \tag{95}$$

where A^f is the fiber area and

$$\frac{\partial \mathbf{C}^f}{\partial \overline{\overline{\mathbf{u}}}_x} = \begin{bmatrix} \frac{\partial C^{(1),f}}{\partial \overline{\overline{u}}_x^{(1)}} & \frac{\partial C^{(1),f}}{\partial \overline{\overline{u}}_x^{(2)}} \\ \frac{\partial C^{(2),f}}{\partial \overline{\overline{u}}_x^{(1)}} & \frac{\partial C^{(2),f}}{\partial \overline{\overline{u}}_x^{(2)}} \end{bmatrix} = \begin{bmatrix} S^{(1)} & 0 \\ 0 & S^{(2)} \end{bmatrix} \tag{96}$$

where $S^{(d)}$ is the softening modulus for the cohesive models defined at integration points. The variables $\mathbf{K}_{G_fG_f}(y, t)$ and $\Delta\overline{\overline{\mathbf{u}}}_x\left(y_f^e, t\right)$

take respectively a matrix and vector form when both discontinuities are simultaneously active on a fiber.

The existence of two discontinuities per fiber necessitates to explain in details the numerical integration of the constitutive laws. The different integration paths are discussed hereafter.

4.2. Numerical integration of the elasto-plastic model and the cohesive model

An elastic prediction (trial) is first made. The cohesive trial stresses $C_{t+1}^{f,(1),trial}$ and $C_{t+1}^{f,(2),trial}$ are written as follows (the enhancement functions $G_v^{(d)}(x)$ were determined in section (2.4) such as the cohesive stress $C^{f,(d)}$ at the discontinuity level is equal to the continuous model stress $\sigma(x_d)$, see Eq. (50)):

$$C_{t+1}^{f,(1),trial} = -\int_{\Omega^f} \overline{G}_v^{(1)}(x)\sigma_{t+1}^{f,trial}(x)d\Omega^f = \sigma_{t+1}^{f,trial}(x_1) \tag{97}$$

$$C_{t+1}^{f,(2),trial} = -\int_{\Omega^f} \overline{G}_v^{(2)}(x)\sigma_{t+1}^{f,trial}(x)d\Omega^f = \sigma_{t+1}^{f,trial}(x_2) \tag{98}$$

Assuming that each fiber is made of a single material and therefore $E(x) = E$, the elastic predictor of the continuous stress $\sigma_{t+1}^{f,trial}(x_{pg})$ is:

$$\sigma_{t+1}^{f,trial}(x_{pg}) = E\varepsilon_{t+1}^{f,trial}(x_{pg}) = E\left[\mathbf{B}^f(x_{pg}, y)\mathbf{d}_{e,t+1} + \overline{\mathbf{G}}_r(x_{pg})\overline{\mathbf{u}}_t - \bar{\varepsilon}_t^p\right] \tag{99}$$

Developing expression (99) for the two integration points gives (calculation details are given in appendices (A.1) and (A.2)) provides:

$$\begin{aligned} C_{t+1}^{f,(1),trial} &= E\left(\mathbf{B}^f(x_1, y)\mathbf{d}_{e,t+1} + \overline{G}_r^{(1)}(x_1)\overline{u}_t(x_1) + \overline{G}_r^{(2)}(x_1)\overline{u}_t(x_2) - \varepsilon_t^p(x_1)\right) \\ C_{t+1}^{f,(2),trial} &= E\left(\mathbf{B}^f(x_2, y)\mathbf{d}_{e,t+1} + \overline{G}_r^{(1)}(x_2)\overline{u}_t(x_1) + \overline{G}_r^{(2)}(x_2)\overline{u}_t(x_2) - \varepsilon_t^p(x_2)\right) \end{aligned} \tag{100}$$

The above stresses (100) are used to calculate the trial failure surfaces $\overline{\phi}_{t+1}^{f,(1),trial}$ and $\overline{\phi}_{t+1}^{f,(2),trial}$ of the vector $\overline{\boldsymbol{\phi}}_{t+1}^{f,trial}$ and therefore to check whether one or both discontinuities are activated:

$$\begin{aligned} \overline{\boldsymbol{\phi}}_{t+1}^{f,trial} &= |\mathbf{C}_{t+1}^{f,trial}| - (\boldsymbol{\sigma}_u - \overline{\mathbf{q}}_{t+1}^{f,trial}) \\ \begin{bmatrix} \overline{\phi}_{t+1}^{f,(1),trial} \\ \overline{\phi}_{t+1}^{f,(1),trial} \end{bmatrix} &= \begin{bmatrix} |C_{t+1}^{f,(1),trial}| - (\sigma_u - \overline{q}_{t+1}^{f,(2),trial}) \\ |C_{t+1}^{f,(2),trial}| - (\sigma_u - \overline{q}_{t+1}^{f,(2),trial}) \end{bmatrix} \end{aligned} \tag{101}$$

Depending on the results, the following situations may occur, see Table 2:

- Case 1: no active discontinuities in the fiber.
- Cases 2 and 3: one active discontinuity in the fiber. Calculation of the internal variables and stresses at the corresponding integration point.
- Case 4: two active discontinuities in the fiber. Calculation of the internal variables and stresses at two integration points.

4.2.1. Two active discontinuities per fiber

The Lagrange multipliers of the two failure surfaces are $\overline{\gamma}(x_1)$ and $\overline{\gamma}(x_2)$. Considering that the cohesive models evolve independently at the two integration points x_1 and x_2 and using a backward Euler numerical integration scheme we get:

$$\begin{aligned} \overline{u}_{t+1}(x_1) &= \overline{u}_t(x_1) + \Delta\overline{\gamma}(x_1)sign(C_{t+1}^{f,(1),trial}) \\ \overline{\xi}_{t+1}(x_1) &= \overline{\xi}_t(x_1) + \Delta\overline{\gamma}(x_1) \end{aligned} \tag{102}$$

and

$$\begin{aligned} \overline{u}_{t+1}(x_2) &= \overline{u}_t(x_2) + \Delta\overline{\gamma}(x_2)sign(C_{t+1}^{f,(2),trial}) \\ \overline{\xi}_{t+1}(x_2) &= \overline{\xi}_t(x_2) + \Delta\overline{\gamma}(x_2) \end{aligned} \tag{103}$$

In order to simplify the expressions, we set $s(x_1) = sign(C_{t+1}^{f,(1),trial})$ and $s(x_2) = sign(C_{t+1}^{f,(2),trial})$. The new stresses at the two

Table 2
Different cases depending on the trial failure surfaces.

Case 1	$\overline{\phi}_{t+1}^{f,(1),trial} < 0$ and $\overline{\phi}_{t+1}^{f,(2),trial} < 0$
Case 2	$\overline{\phi}_{t+1}^{f,(1),trial} > 0$ and $\overline{\phi}_{t+1}^{f,(2),trial} < 0$
Case 3	$\overline{\phi}_{t+1}^{f,(1),trial} < 0$ and $\overline{\phi}_{t+1}^{f,(2),trial} > 0$
Case 4	$\overline{\phi}_{t+1}^{f,(1),trial} > 0$ and $\overline{\phi}_{t+1}^{f,(2),trial} > 0$

integration points become (see Appendix A.3 for the details):

$$C_{t+1}^{f,(1)} = \sigma_{t+1}^{trial}(x_1) + E\overline{G}_r^{(1)}(x_1)\Delta\overline{\gamma}(x_1)s(x_1) + E\overline{G}_r^{(2)}(x_1)\Delta\overline{\gamma}(x_2)s(x_2)$$
$$C_{t+1}^{f,(2)} = \sigma_{t+1}^{trial}(x_2) + E\overline{G}_r^{(1)}(x_2)\Delta\overline{\gamma}(x_1)s(x_1) + E\overline{G}_r^{(2)}(x_2)\Delta\overline{\gamma}(x_2)s(x_2) \tag{104}$$

Eq. (104) can be written in a matrix form as follows:

$$\begin{bmatrix}\sigma_{t+1}(x_1)\\ \sigma_{t+1}(x_2)\end{bmatrix} = \begin{bmatrix}\sigma_{t+1}^{trial}(x_1)\\ \sigma_{t+1}^{trial}(x_2)\end{bmatrix} + \begin{bmatrix}E\overline{G}_r^{(1)}(x_1)s(x_1) & E\overline{G}_r^{(2)}(x_1)s(x_2)\\ E\overline{G}_r^{(1)}(x_2)s(x_1) & E\overline{G}_r^{(2)}(x_2)s(x_2)\end{bmatrix}\begin{bmatrix}\Delta\overline{\gamma}(x_1)\\ \Delta\overline{\gamma}(x_2)\end{bmatrix} \tag{105}$$

$\Delta\overline{\gamma}(x_1)$ and $\Delta\overline{\gamma}(x_2)$ are determined introducing (105) in the failure surfaces (that are equal to zero). This gives (see Appendix (A.5) for the details):

$$\begin{bmatrix}\Delta\overline{\gamma}(x_1)\\ \Delta\overline{\gamma}(x_2)\end{bmatrix} = -\begin{bmatrix}E\overline{G}_r^{(1)}(x_1) - S & E\overline{G}_r^{(2)}(x_1)s(x_2)s(x_1)\\ E\overline{G}_r^{(1)}(x_2)s(x_1)s(x_2) & E\overline{G}_r^{(2)}(x_2) - S\end{bmatrix}^{-1}\begin{bmatrix}\overline{\phi}_{t+1}^{trial}(x_1)\\ \overline{\phi}_{t+1}^{trial}(x_2)\end{bmatrix} \tag{106}$$

According to Eq. (106), the calculation of Lagrange multipliers is interdependent. This means numerically that the calculation for both discontinuities will take place simultaneously and not successively. The final step consists in updating the internal variables following Eqs. (102) and (103).

4.2.2. Complete failure at the two discontinuities

If both discontinuities are fully open, the two failure surfaces become zero ($\sigma_u - \overline{q}_{t+1}(x_{pg}) = 0$) and no stress transfer occurs. Both cohesive stresses are therefore zero and this results to (see Appendix (A.6) for the details):

$$\begin{bmatrix}\Delta\overline{\gamma}(x_1)\\ \Delta\overline{\gamma}(x_2)\end{bmatrix} = -\begin{bmatrix}E\overline{G}_r^{(1)}(x_1)s(x_1) & E\overline{G}_r^{(2)}(x_1)s(x_2)\\ E\overline{G}_r^{(1)}(x_2)s(x_1) & E\overline{G}_r^{(2)}(x_2)s(x_2)\end{bmatrix}^{-1}\begin{bmatrix}\sigma_{t+1}^{trial}(x_1)\\ \sigma_{t+1}^{trial}(x_2)\end{bmatrix} \tag{107}$$

4.2.3. Complete failure at one discontinuity

For the case of a complete failure at one discontinuity, the corresponding cohesive stress cancels out while the other discontinuity continues its opening process. Two equations have to be used, the first corresponding to the fully open discontinuity ($\sigma_{t+1}(x_1) = 0$) and the second resulting from the failure surface $\overline{\phi}_{t+1}$ of the still evolving discontinuity. This gives the following system:

$$\begin{cases}\sigma_{t+1}(x_1) = 0\\ \overline{\phi}_{t+1}(x_2) = 0\end{cases} \tag{108}$$

The first equation is similar to the first equation of the system in Eq. (107), while the second equation is the one in Eq. (106). We finally get (see Appendix (A.7) for the details):

$$\begin{bmatrix}\Delta\overline{\gamma}(x_1)\\ \Delta\overline{\gamma}(x_2)\end{bmatrix} = -\begin{bmatrix}E\overline{G}_r^{(1)}(x_1)s(x_1) & E\overline{G}_r^{(2)}(x_1)s(x_2)\\ E\overline{G}_r^{(1)}(x_2)s(x_1)s(x_2) & E\overline{G}_r^{(2)}(x_2) - S\end{bmatrix}^{-1}\begin{bmatrix}\sigma_{t+1}^{trial}(x_1)\\ \overline{\phi}_{t+1}^{trial}(x_2)\end{bmatrix} \tag{109}$$

4.3. Numerical integration of the damage mechanics model and the cohesive model

The numerical integration of the damage mechanics model associated with the cohesive model is presented hereafter. The evolution of the internal variables of each discontinuity is independent. Nevertheless, the calculation of strains and stresses as well as the corresponding Lagrange multipliers are coupled. Therefore, equations illustrating the evolution of the cohesive variables are hereafter adopted for each discontinuity.

The particularity of the damage model lies in the fact that the trial values of the displacement jumps ($\overline{\mathbf{u}}_{t+1}^{trial}(x_1)$ and $\overline{\mathbf{u}}_{t+1}^{trial}(x_2)$) at the discontinuities at time step $t+1$ are not the same as the ones ($\overline{\mathbf{u}}_t(x_1)$ and $\overline{\mathbf{u}}_t(x_2)$) of the previous time step t (this remark is important for a successful numerical implementation of the model). Indeed,

$$\overline{\mathbf{u}}_{t+1}^{trial}(x_1) = \overline{D}_{t+1}^{trial}(x_1)C_{t+1}^{f,(1),trial} = \overline{D}_t(x_1)\sigma_{t+1}^{trial}(x_1) \neq \overline{D}_t(x_1)\sigma_t(x_1) = \overline{\mathbf{u}}_t(x_1)$$
$$\overline{\mathbf{u}}_{t+1}^{trial}(x_2) = \overline{D}_{t+1}^{trial}(x_2)C_{t+1}^{f,(2),trial} = \overline{D}_t(x_2)\sigma_{t+1}^{trial}(x_2) \neq \overline{D}_t(x_2)\sigma_t(x_2) = \overline{\mathbf{u}}_t(x_2) \tag{110}$$

The first step is the elastic prediction of stresses. We obtain the following system (see Appendix B for the details):

$$\begin{bmatrix}\sigma_{t+1}^{trial}(x_1)\\ \sigma_{t+1}^{trial}(x_2)\end{bmatrix} = \begin{bmatrix}\overline{D}_t^{-1}(x_1)\overline{G}_r^{(1)}(x_1)\overline{D}_t(x_1) - 1 & \overline{D}_t^{-1}(x_1)\overline{G}_r^{(2)}(x_1)\overline{D}_t(x_2)\\ \overline{D}_t^{-1}(x_2)\overline{G}_r^{(1)}(x_2)\overline{D}_t(x_1) & \overline{D}_t^{-1}(x_2)\overline{G}_r^{(2)}(x_2)\overline{D}_t(x_2) - 1\end{bmatrix}^{-1}\begin{bmatrix}-\overline{D}_t^{-1}(x_1)\mathbf{B}^f(x_1,y)\mathbf{d}_{e,t+1}\\ -\overline{D}_t^{-1}(x_2)\mathbf{B}^f(x_2,y)\mathbf{d}_{e,t+1}\end{bmatrix} \tag{111}$$

showing that elastic predictions of the stress states at the integration points are coupled.

The next step is to introduce the calculated stresses in the failure surfaces $\overline{\overline{\phi}}_{t+1}^{trial}(x_1)$ and $\overline{\overline{\phi}}_{t+1}^{trial}(x_2)$:

$$\begin{bmatrix} \overline{\overline{\phi}}_{t+1}^{trial}(x_1) \\ \overline{\overline{\phi}}_{t+1}^{trial}(x_2) \end{bmatrix} = \begin{bmatrix} |\sigma_{t+1}^{trial}(x_1)| \\ |\sigma_{t+1}^{trial}(x_2)| \end{bmatrix} - \begin{bmatrix} \sigma_u - \overline{\overline{q}}_t(x_1) \\ \sigma_u - \overline{\overline{q}}_t(x_2) \end{bmatrix}. \tag{112}$$

and the stress vector of Eq. (111) in Eq. (112):

$$\begin{bmatrix} \overline{\overline{\phi}}_{t+1}^{trial}(x_1) \\ \overline{\overline{\phi}}_{t+1}^{trial}(x_2) \end{bmatrix} = \begin{bmatrix} \overline{D}_t^{-1}(x_1)\overline{G}_r^{(1)}(x_1)\overline{\overline{D}}_t(x_1) - 1 & \overline{D}_t^{-1}(x_1)\overline{G}_r^{(2)}(x_1)\overline{\overline{D}}_t(x_2)s(x_1)s(x_2) \\ \overline{D}_t^{-1}(x_2)\overline{G}_r^{(1)}(x_2)\overline{\overline{D}}_t(x_1)s(x_1)s(x_2) & \overline{D}_t^{-1}(x_2)\overline{G}_r^{(2)}(x_2)\overline{\overline{D}}_t(x_2) - 1 \end{bmatrix}^{-1} \times \begin{bmatrix} -\overline{D}_t^{-1}(x_1)\mathbf{B}^f(x_1, y)\mathbf{d}_{e,t+1}s(x_1) \\ -\overline{D}_t^{-1}(x_2)\mathbf{B}^f(x_2, y)\mathbf{d}_{e,t+1}s(x_2) \end{bmatrix} - \begin{bmatrix} \sigma_t(x_1) \\ \sigma_t(x_2) \end{bmatrix} \tag{113}$$

The different cases presented in Section 4.2 and Table 2 are found.

4.3.1. Two active discontinuities per fiber

The two failure surfaces ($\overline{\overline{\phi}}_{t+1}^{trial}(x_1)$and $\overline{\overline{\phi}}_{t+1}^{trial}(x_2)$) are positive. The internal variables associated with the continuous damage model are thus frozen while the internal variables associated with the cohesive model must be updated. The new stresses obtained at the integration points take the following form (see Appendices (B.5) and (B.6) for the calculation details):

$$\begin{aligned} \begin{bmatrix} \sigma_{t+1}(x_1) \\ \sigma_{t+1}(x_2) \end{bmatrix} = & \begin{bmatrix} \overline{D}_t^{-1}(x_1)\mathbf{B}^f(x_1, y)\mathbf{d}_{e,t+1} \\ \overline{D}_t^{-1}(x_2)\mathbf{B}^f(x_2, y)\mathbf{d}_{e,t+1} \end{bmatrix} + \begin{bmatrix} \overline{D}_t^{-1}(x_1)\overline{G}_r^{(1)}(x_1)\overline{\overline{D}}_t(x_1)s(x_1) & \overline{D}_t^{-1}(x_1)\overline{G}_r^{(2)}(x_1)\overline{\overline{D}}_t(x_2)s(x_2) \\ \overline{D}_t^{-1}(x_2)\overline{G}_r^{(1)}(x_2)\overline{\overline{D}}_t(x_1)s(x_1) & \overline{D}_t^{-1}(x_2)\overline{G}_r^{(2)}(x_2)\overline{\overline{D}}_t(x_2)s(x_2) \end{bmatrix} \begin{bmatrix} \sigma_t(x_1) \\ \sigma_t(x_2) \end{bmatrix} \\ & + \begin{bmatrix} \overline{D}_t^{-1}(x_1)\overline{G}_r^{(1)}(x_1)s(x_1) & \overline{D}_t^{-1}(x_1)\overline{G}_r^{(2)}(x_1)s(x_2) \\ \overline{D}_t^{-1}(x_2)\overline{G}_r^{(1)}(x_2)s(x_1) & \overline{D}_t^{-1}(x_2)\overline{G}_r^{(2)}(x_2)s(x_2) \end{bmatrix} \begin{bmatrix} \Delta\overline{\overline{\gamma}}(x_1) \\ \Delta\overline{\overline{\gamma}}(x_2) \end{bmatrix} \end{aligned} \tag{114}$$

In order to determine the Lagrange multipliers $\Delta\overline{\overline{\gamma}}(x_1)$ and $\Delta\overline{\overline{\gamma}}(x_2)$, Eq. (114) are introduced to the failure surfaces:

$$\begin{matrix} \overline{\overline{\phi}}_{t+1}(x_1) = 0 \\ \overline{\overline{\phi}}_{t+1}(x_2) = 0 \end{matrix} \quad \Leftrightarrow \quad \begin{bmatrix} |\sigma_{t+1}(x_1)| \\ |\sigma_{t+1}(x_2)| \end{bmatrix} - \begin{bmatrix} \sigma_u - \overline{\overline{q}}_{t+1}(x_1) \\ \sigma_u - \overline{\overline{q}}_{t+1}(x_2) \end{bmatrix} = \begin{bmatrix} 0 \\ 0 \end{bmatrix} \tag{115}$$

The Lagrange multipliers are calculated as follows (see Appendix B.1.1 for the details):

$$\begin{aligned} \begin{bmatrix} \Delta\overline{\overline{\gamma}}(x_1) \\ \Delta\overline{\overline{\gamma}}(x_2) \end{bmatrix} = & \begin{bmatrix} \overline{D}_t^{-1}(x_1)\overline{G}_r^{(1)}(x_1) - S & \overline{D}_t^{-1}(x_1)\overline{G}_r^{(2)}(x_1)s(x_2)s(x_1) \\ \overline{D}_t^{-1}(x_2)\overline{G}_r^{(1)}(x_2)s(x_1)s(x_2) & \overline{D}_t^{-1}(x_2)\overline{G}_r^{(2)}(x_2) - S \end{bmatrix}^{-1} \\ & \times \begin{bmatrix} \overline{D}_t^{-1}(x_1)\overline{G}_r^{(1)}(x_1)\overline{\overline{D}}_t(x_1) - 1 & \overline{D}_t^{-1}(x_1)\overline{G}_r^{(2)}(x_1)\overline{\overline{D}}_t(x_2)s(x_2)s(x_1) \\ \overline{D}_t^{-1}(x_2)\overline{G}_r^{(1)}(x_2)\overline{\overline{D}}_t(x_1)s(x_1)s(x_2) & \overline{D}_t^{-1}(x_2)\overline{G}_r^{(2)}(x_2)\overline{\overline{D}}_t(x_2) - 1 \end{bmatrix} \begin{bmatrix} \overline{\overline{\phi}}_{t+1}^{trial}(x_1) \\ \overline{\overline{\phi}}_{t+1}^{trial}(x_2) \end{bmatrix} \end{aligned} \tag{116}$$

The internal variables associated with the cohesive models are finally updated.

4.3.2. Complete failure at the two discontinuities

When both discontinuities are fully open, we have:

$$\begin{bmatrix} \sigma_{t+1}(x_1) \\ \sigma_{t+1}(x_2) \end{bmatrix} = \begin{bmatrix} 0 \\ 0 \end{bmatrix} \tag{117}$$

It can be found (see Appendix B.3 for the details):

$$\begin{aligned} \begin{bmatrix} \Delta\overline{\overline{\gamma}}(x_1) \\ \Delta\overline{\overline{\gamma}}(x_2) \end{bmatrix} - = & \begin{bmatrix} \overline{D}_t^{-1}(x_1)\overline{G}_r^{(1)}(x_1)s(x_1) & \overline{D}_t^{-1}(x_1)\overline{G}_r^{(2)}(x_1)s(x_2) \\ \overline{D}_t^{-1}(x_2)\overline{G}_r^{(1)}(x_2)s(x_1) & \overline{D}_t^{-1}(x_2)\overline{G}_r^{(2)}(x_2)s(x_2) \end{bmatrix}^{-1} \times \left(\begin{bmatrix} \overline{D}_t^{-1}(x_1)\mathbf{B}^f(x_1, y)\mathbf{d}_{e,t+1} \\ \overline{D}_t^{-1}(x_2)\mathbf{B}^f(x_2, y)\mathbf{d}_{e,t+1} \end{bmatrix} \right. \\ & \left. + \begin{bmatrix} \overline{D}_t^{-1}(x_1)\overline{G}_r^{(1)}(x_1)\overline{\overline{D}}_t(x_1)s(x_1) & \overline{D}_t^{-1}(x_1)\overline{G}_r^{(2)}(x_1)\overline{\overline{D}}_t(x_2)s(x_2) \\ \overline{D}_t^{-1}(x_2)\overline{G}_r^{(1)}(x_2)\overline{\overline{D}}_t(x_1)s(x_1) & \overline{D}_t^{-1}(x_2)\overline{G}_r^{(2)}(x_2)\overline{\overline{D}}_t(x_2)s(x_2) \end{bmatrix} [\sigma_t(x_1)\sigma_t(x_2)] \right) \end{aligned} \tag{118}$$

4.3.3. Complete failure at a one discontinuity

As in Section 4.2.3, the following system is found:

$$\begin{cases} \sigma_{t+1}(x_1) = 0 \\ \overline{\overline{\phi}}_{t+1}(x_2) = 0 \end{cases} \tag{119}$$

The corresponding Lagrange multipliers are:

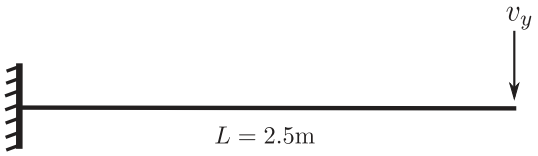

Fig. 7. Cantilever beam structure submitted to a transverse displacement.

$$\begin{bmatrix}\Delta\overline{\overline{\gamma}}(x_1)\\ \Delta\overline{\overline{\gamma}}(x_2)\end{bmatrix} = -\begin{bmatrix}\overline{D}_t^{-1}(x_1)\overline{G}_r^{(1)}(x_1)s(x_1) & \overline{D}_t^{-1}(x_1)\overline{G}_r^{(2)}(x_1)s(x_2)\\ \overline{D}_t^{-1}(x_2)\overline{G}_r^{(1)}(x_2)s(x_1)s(x_2) & \overline{D}_t^{-1}(x_2)\overline{G}_r^{(2)}(x_2) - S\end{bmatrix}^{-1} \times \left(\begin{bmatrix}\overline{D}_t^{-1}(x_1)\mathbf{B}^f(x_1,y)\mathbf{d}_{e,t+1}\\ \overline{D}_t^{-1}(x_2)\mathbf{B}^f(x_2,y)\mathbf{d}_{e,t+1}s(x_2)\end{bmatrix} + \begin{bmatrix}\overline{D}_t^{-1}(x_1)\overline{G}_r^{(1)}(x_1)\overline{\overline{D}}_t(x_1)s(x_1) & \overline{D}_t^{-1}(x_1)\overline{G}_r^{(2)}(x_1)\overline{\overline{D}}_t(x_2)s(x_2)\\ \overline{D}_t^{-1}(x_2)\overline{G}_r^{(1)}(x_2)\overline{\overline{D}}_t(x_1)s(x_1)s(x_2) & \overline{D}_t^{-1}(x_2)\overline{G}_r^{(2)}(x_2)\overline{\overline{D}}_t(x_2) - 1\end{bmatrix}\begin{bmatrix}\sigma_t(x_1)\\ \sigma_t(x_2)\end{bmatrix}\right) \tag{120}$$

For the case when a constant stress/strain occurs in the fiber the choice made is to allow only one discontinuity.

5. Numerical applications

In order to validate the numerical implementation of the higher order enhanced Timoshenko multifiber beam and to study its performance, two numerical applications are presented: (1) a cantilever beam structure (2) a reinforced concrete framed structure tested by [58] and simulated in [59,60].

5.1. Cantilever beam structure

A cantilever beam structure of length $L = 2.5$ m submitted to a transverse displacement v_y at its free end is studied hereafter, see Fig. 7. The aim of this example is to prove the numerical efficiency of the higher order multifiber beam (**FCQ**) and to compare its performance with first order multifiber beams (**FLI**) existing in the literature [40].

A first case is considered where the fibers are not enhanced and follow a bilinear softening constitutive law (Fig. 8a). Symmetrical thresholds are considered in tension and compression. Then, a second case is studied with a linear elastic constitutive law coupled with a linear cohesive model (Fig. 8b). The material properties are summarized in Table 3.

The structure is discretized with different number (NE) of **FLI** or **FCQ** multifiber Timoshenko beams. Each section is discretized with 20 fibers. Results are presented in Fig. 9.

Fig. 9 illustrates the effect of mesh refinement on the global (bending moment – transversal imposed displacement) structural response considering or not fiber enhancement. Without enhancement, the results of the **FLI** and **FCQ** elements are similar and depend on the mesh size, see Fig. 9a and b. Fig. 9a and c show that the fiber enhancement improves the **FLI** performance. Nevertheless, mesh dependency is still significant in terms of softening response but also ultimate moment. Finally, Fig. 9b and d clearly show that the fiber enhancement of the **FCQ** Timoshenko beams makes the answer (almost) identical, independent of the number of elements.

5.2. Reinforced concrete frame

The non linear behavior of a reinforced concrete frame is studied hereafter. The frame has been tested by [58] and numerically modeled by several authors using classical finite elements [61,59] or **FLI** multifiber Timoshenko beam elements [22]. The frame geometry is illustrated in Fig. 10. The geometry and the applied loading being symmetric, half of the frame is considered for the numerical model. All frame sections are of rectangular shape with a height $h = 0.1524$ m and width $b = 0.1016$ m. The top and bottom fiber concrete covering is 0.014 m. The steel reinforcement is shown in Fig. 10.

Concrete fibers are modeled with the damage model presented in Section 3.1.1. The steel fibers are modeled with the elasto-

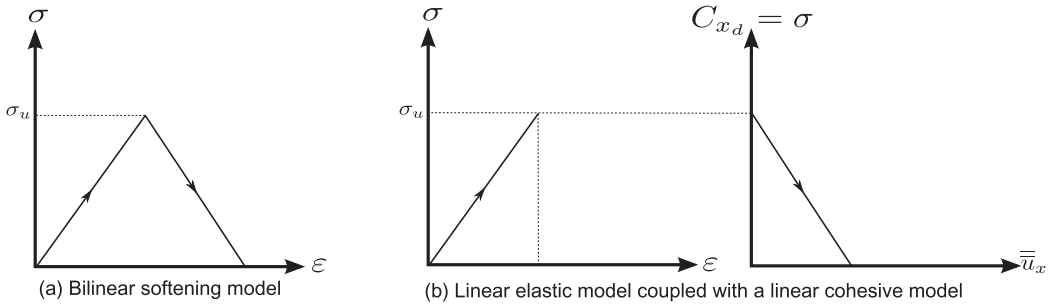

(a) Bilinear softening model (b) Linear elastic model coupled with a linear cohesive model

Fig. 8. Constitutive laws (a) case without enhancement (b) case with enhancement.

Table 3
Material properties.

Properties	Symbol	Value
Young modulus	E	4×10^7 kN m^{-2}
Poisson coefficient	ν	0.2
Softening modulus	S	-8×10^5 kN m^{-3}
Ultimate elastic stress	σ_u	5000 kN m^{-2}

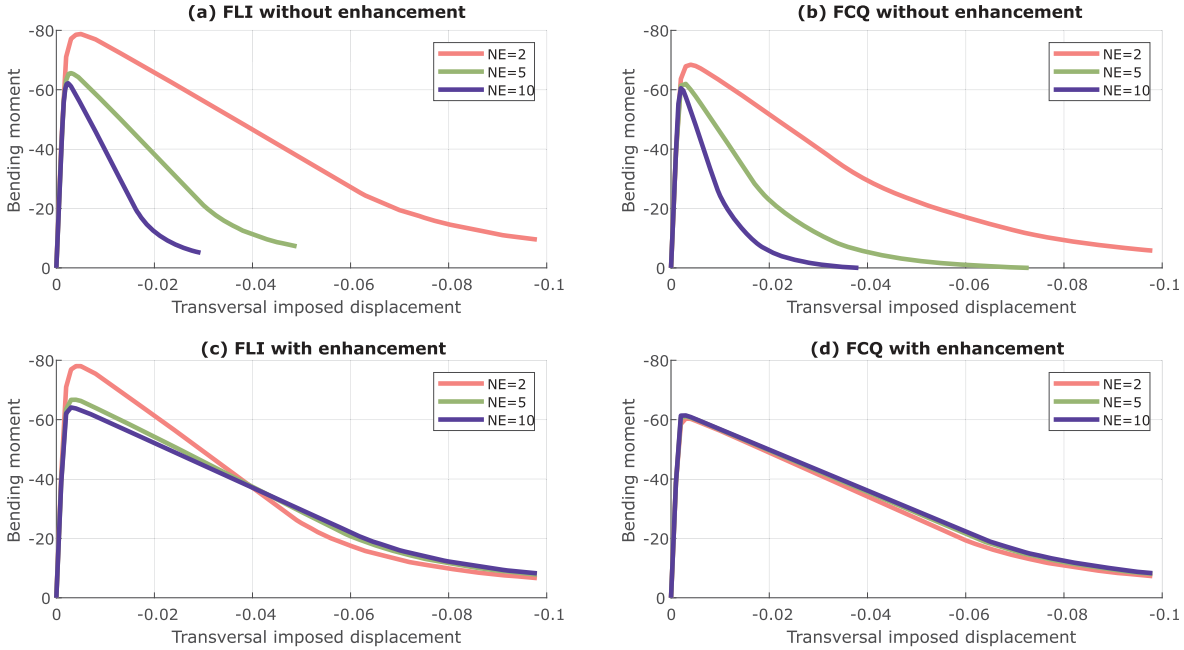

Fig. 9. Cantilever beam structure – Bending moment versus transversal imposed displacement as a function of the number (NE) and type (**FLI** or **FCQ**) of multifiber Timoshenko beam elements.

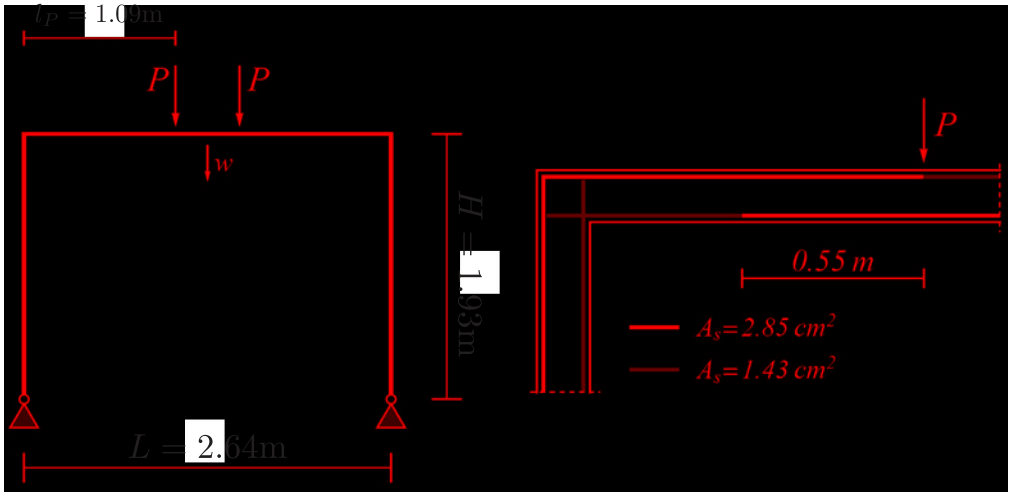

Fig. 10. Reinforced concrete frame tested by Cranston [58].

plastic model of Section 3.2.1. Both damage and elasto-plastic models are coupled with cohesive models (Sections 3.1.2 and 3.2.2 respectively) in order to describe the material behaviour at the discontinuities level, i.e. the integration points. Concrete and steel properties are summarized in the Tables 4 and 5.

The frame is modeled using only 5 **FCQ** multifiber Timoshenko beam elements (NE = 5): two elements for the column and three

Table 4
Reinforced concrete frame – Concrete properties.

Properties	Symbol	Value
Young modulus	E_b	31.5×10^6 kN m^{-2}
Poisson's coefficient	ν_b	0.2
Ultimate stress in traction	σ_{btu}	950 kN m^{-2}
Elastic stress in compression	σ_{bcy}	14,600 kN m^{-2}
Ultimate stress in compression	σ_{bcu}	36,500 kN m^{-2}
Hardening modulus in compression	H_{bc}	29×10^6 kN m^{-2}
Softening modulus in compression	S_{bc}	-40×10^6 kN m^{-3}
Softening modulus in tension	S_{bt}	-11×10^6 kN m^{-3}

Table 5
Reinforced concrete frame – Steel properties.

Properties	Symbol	Value
Young Modulus	E_a	200×10^6 kNm^{-2}
Poisson's coefficient	ν_a	0.3
Elastic stress limit	σ_{ay}	293,000 kN m^{-2}
Ultimate stress	σ_{au}	310,000 kN m^{-2}
Hardening modulus	H_a	5.02×10^5 kN m^{-2}
Softening modulus	S_a	-42×10^6 kNm^{-3}

elements for the beam. Each section is discretized with 20 fibers (18 for concrete and 2 for steel). The thickness of the steel fibers is calculated by respecting the steel ratio of the section, given in Fig. 10. Perfect bonding is considered between steel and concrete and 3D phenomena – as concrete confinement due to the stirrups – are not taken into account. In Fig. 11 (right), the notation $S(e, g)$ means the section S at the integration point g of element e. Also, f(i) denotes the fiber of number i. Due to the symmetric configuration of the frame structure (see Fig. 10, left), only half of it is simulated (see Fig. 10, right) and thus a vertical increasing displacement v_y is imposed as shown in Fig. 11.

The global response (force versus applied vertical displacement) of the frame is illustrated in Fig. 12. Results of the NE = 5 **FCQ** multifiber Timoshenko beams model are compared with experimental results [58], classical finite element results [61] and the NE = 104 **FLI** multifiber Timoshenko beams model [22]. The **FCQ** model response is in good agreement with the experimental results

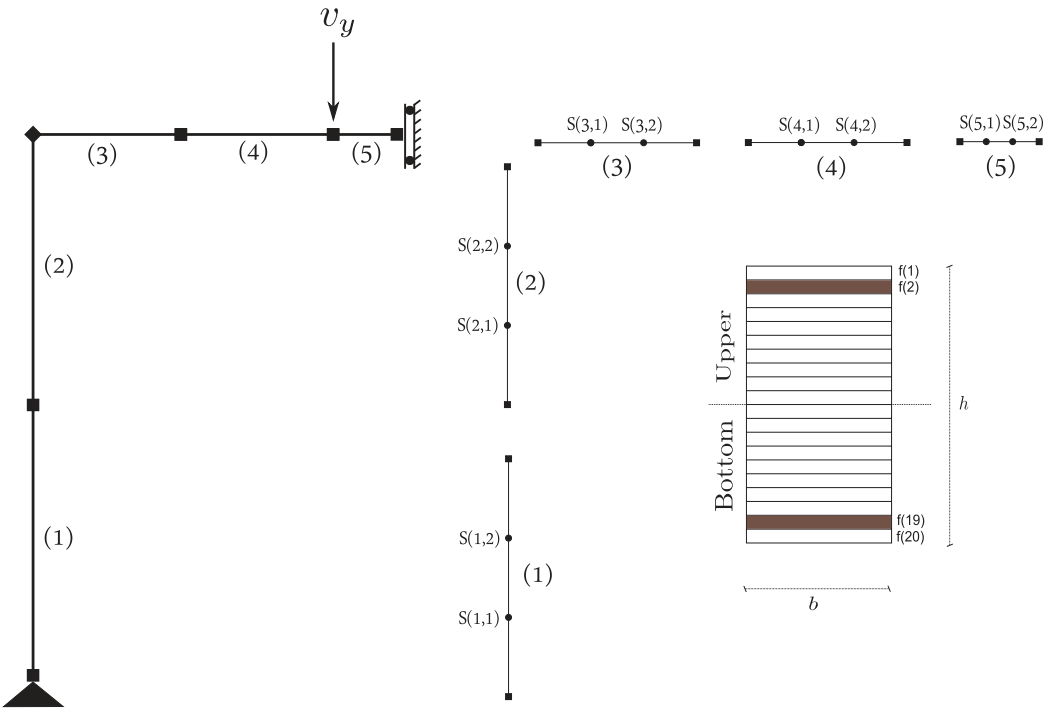

Fig. 11. Reinforced concrete frame – Detail of the frame (left) and cross section (right) meshes.

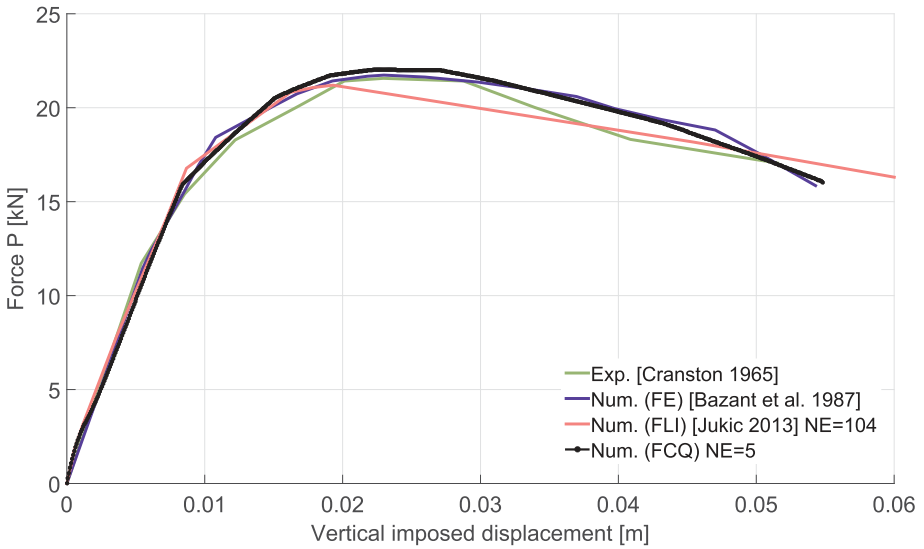

Fig. 12. Reinforced concrete frame – Force versus vertical imposed displacement: experimental, finite elements (FE), **FLI** and **FCQ** model results.

[58] and the finite element numerical results [61]. The **FLI** model results are less accurate, despite the important number of beam elements adopted.

In order to analyze the local behaviour at the fiber level and to see how it affects the global response, the results of the **FCQ** model are isolated in Fig. 13. The force/displacement coordinates of the points A-G in Fig. 13 are summarized in Table 6. Each point corresponds to a local phenomenon that affects the global response of the structure. More specifically:

- Point A corresponds to the first change of the slope. It is related to the beginning of the hardening phase of the lower steel fiber in element 5 (see Fig. 14c).
- Point B corresponds to the same fiber when it reaches its ultimate stress (310 MPa), see Fig. 14c.
- Point C denotes the beginning of hardening of the upper steel fiber in Section 2 of the upper steel fiber (S(2,2)/f (2), Fig. 11) of element 2 (Fig. 14a).
- Point D corresponds to the hardening of Section 1 (S(3,1), Fig. 11) of the upper steel fiber (f(2), Fig. 11) of element 3.
- Points E and F represent the beginning of hardening of the upper steel fibers f(2) of sections S(2,1) and S(3,2) of elements 2 and 3 respectively.
- Point G indicates the time step where the top-steel fibers of sections S(2,2) and S(3,1) of elements 2 and 3 reach their ultimate values (σ_{su} = 310 MPa).

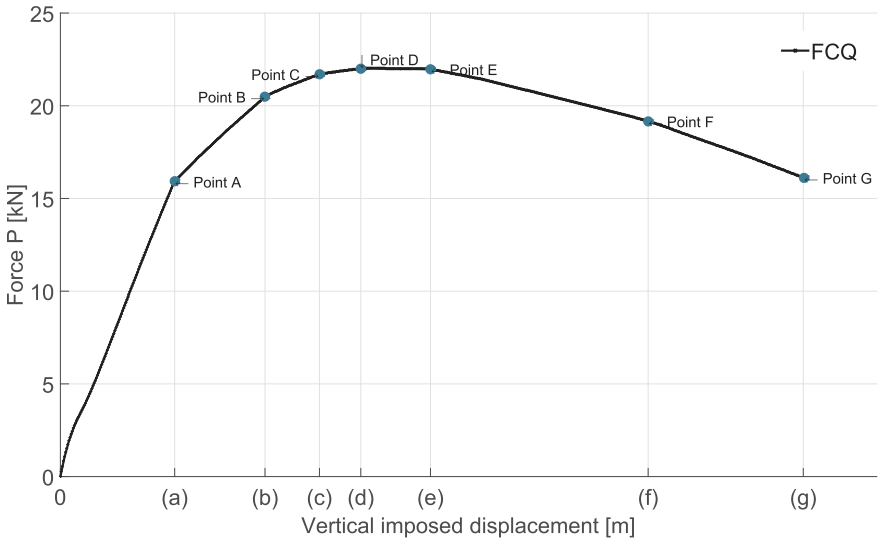

Fig. 13. Reinforced concrete frame – Force versus vertical imposed displacement: **FCQ** model results.

Table 6

Reinforced concrete frame – The coordinates of the green points on the Fig. 13.

Point	0	A	B	C	D	E	F	G
v_y (m)	0	0.0084	0.01504	0.01904	0.02208	0.0272	0.0432	0.0546
F_y (kN)	0	15.93	20.49	21.71	22.51	21.98	19.17	16.12

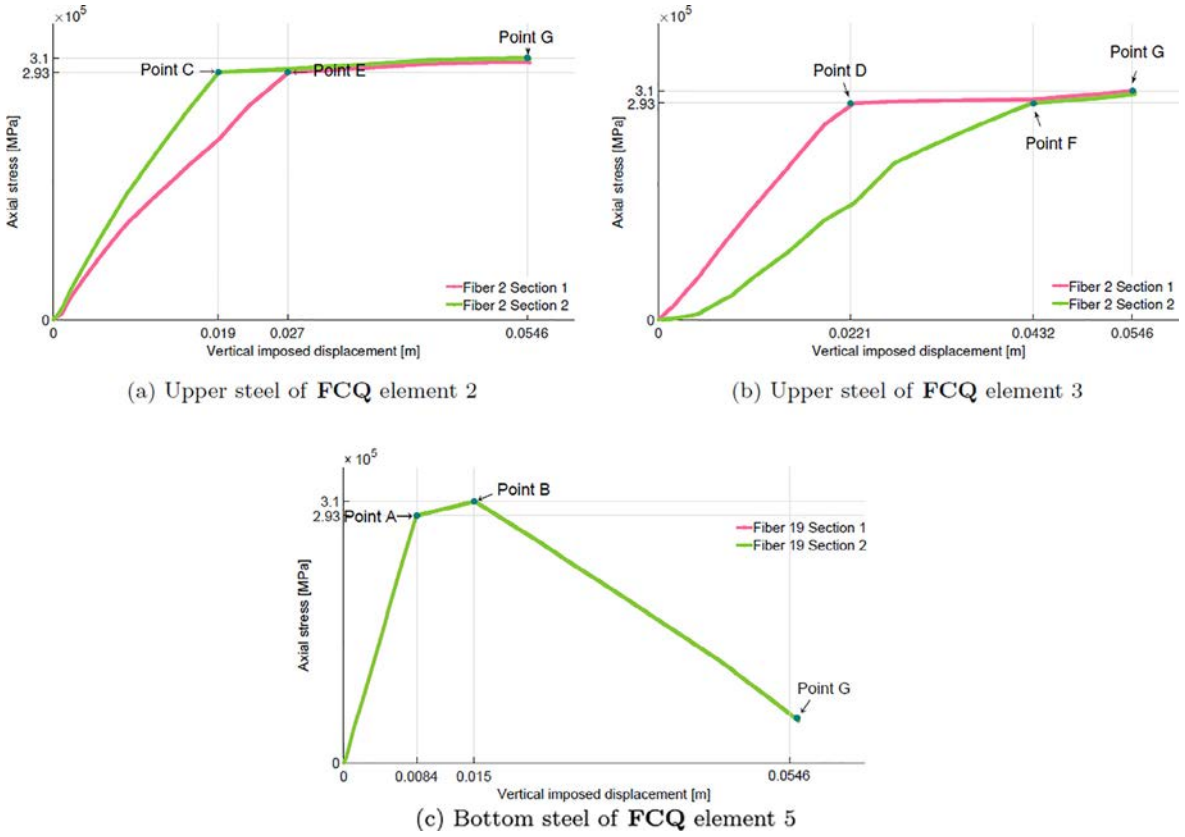

Fig. 14. Reinforced concrete frame – Evolution of stress in the fibers, **FCQ** model.

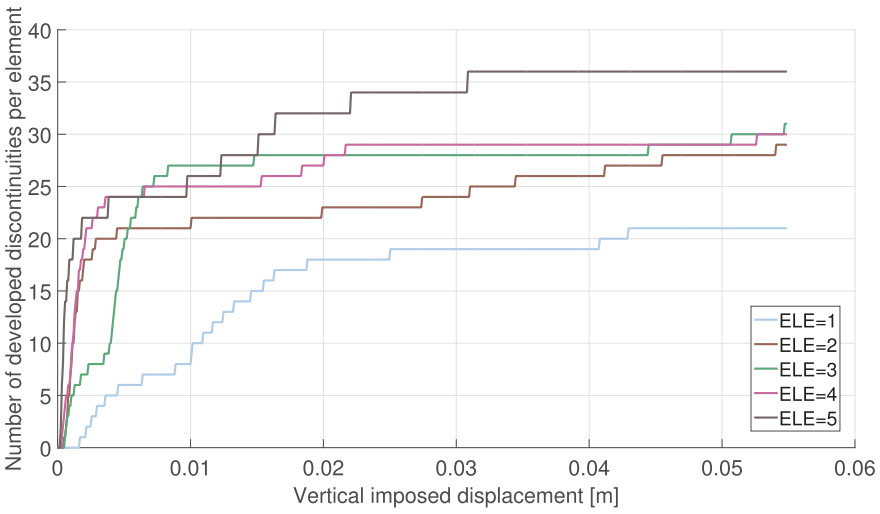

Fig. 15. The number of discontinuities developed per element as a function of the imposed displacement.

Following the previous analysis, the behaviour of the steel fibers dominates the global reinforced concrete frame response. Nevertheless, discontinuities in concrete fibres start developing from the very beginning. Indeed, Fig. 15 illustrates the number of fibers with discontinuities developed in each element (ELE) as a function of the imposed vertical displacement. This numerical study proves the ability of the higher order multifiber **FCQ** Timoshenko beam to reproduce the non linear behavior of realistic reinforced concrete structures and to follow the evolution of non-linearities both at global and local levels, reason for considering it as a high valuable multi-scale numerical tool.

6. Conclusion

A novel high order enhanced multifiber Timoshenko beam is introduced in this article. The element is based on the Timoshenko finite element beam formulation of [23]. The novelty of the enhanced beam lies in its ability to reproduce several discontinuities along the fibers ensuring compliance with the stress limit values. The variational formulation, the constitutive models and several computational issues are covered. Numerical examples are given to validate the model and to study its performance.

As a perspective of this work, one can mention the enhancement of the transverse component of the displacement field at the fiber level in order to study torsion or shear problems. Coupling between axial and transverse discontinuities can be also useful to simulate two-dimensional softening behaviour at the fiber level. Finally, extension of the model for cyclic and dynamic loadings requires to take into account crack opening and closure.

Acknowledgments

The authors would like to thank the PIA-SINAPS@ project (Sésisme et Installation Nucléaire: Améliorer et Pérenniser la Sureté), approved and funded by the National Agency of Research (ANR) following the RSNR 2012 call for projects on future investments post-Fukoshima. (SINAPS@ ANR-11-RSNR-0022).

Appendix A. Integration of the cohesive elasto-plastic model

First, the trial values of the cohesive stresses (100) are obtained in the following way:

$$\begin{aligned} C_{t+1}^{f,(1),trial} &= \sigma_{t+1}^{trial}(x_1) = E(\varepsilon_{t+1}^{trial}(x_1) - \varepsilon_t^p(x_1)) = E(\mathbf{B}^f(x_1, y)\mathbf{d}_{e,t+1} + \overline{G}_r^{(1)}(x_1)\overline{\overline{u}}_{t+1}^{trial}(x_1) + \overline{G}_r^{(2)}(x_1)\overline{\overline{u}}_{t+1}^{trial}(x_2) - \varepsilon_t^p(x_1)) \\ &= E(\mathbf{B}^f(x_1, y)\mathbf{d}_{e,t+1} + \overline{G}_r^{(1)}(x_1)\overline{\overline{u}}_t(x_1) + \overline{G}_r^{(2)}(x_1)\overline{\overline{u}}_t(x_2) - \varepsilon_t^p(x_1)) \end{aligned} \tag{A.1}$$

$$\begin{aligned} C_{t+1}^{f,(2),trial} &= \sigma_{t+1}^{trial}(x_2) = E(\varepsilon_{t+1}^{trial}(x_2) - \varepsilon_t^p(x_2)) = E(\mathbf{B}^f(x_2, y)\mathbf{d}_{e,t+1} + \overline{G}_r^{(1)}(x_2)\overline{\overline{u}}_{t+1}^{trial}(x_1) + \overline{G}_r^{(2)}(x_2)\overline{\overline{u}}_{t+1}^{trial}(x_2) - \varepsilon_t^p(x_2)) \\ &= E(\mathbf{B}^f(x_2, y)\mathbf{d}_{e,t+1} + \overline{G}_r^{(1)}(x_2)\overline{\overline{u}}_t(x_1) + \overline{G}_r^{(2)}(x_2)\overline{\overline{u}}_t(x_2) - \varepsilon_t^p(x_2)) \end{aligned} \tag{A.2}$$

A.1. Two active discontinuities per fiber

For the case of two active discontinuities per fiber, the new values of the cohesive stresses (104) are:

$$\begin{aligned} C_{t+1}^{f,(1)} &= \sigma_{t+1}(x_1) = E(\varepsilon_{t+1}(x_1) - \varepsilon_t^p(x_1)) = E(\mathbf{B}^f(x_1, y)\mathbf{d}_{e,t+1} + \overline{G}_r^{(1)}(x_1)\overline{\overline{u}}_{t+1}(x_1) + \overline{G}_r^{(2)}(x_1)\overline{\overline{u}}_{t+1}(x_2) - \varepsilon_t^p(x_1)) \\ &= \sigma_{t+1}^{trial}(x_1) + E\overline{G}_r^{(1)}(x_1)\Delta\overline{\overline{u}}(x_1) + E\overline{G}_r^{(2)}(x_1)\Delta\overline{\overline{u}}(x_2) = \sigma_{t+1}^{trial}(x_1) + E\overline{G}_r^{(1)}(x_1)\Delta\overline{\overline{\gamma}}(x_1)s(x_1) + E\overline{G}_r^{(2)}(x_1)\Delta\overline{\overline{\gamma}}(x_2)s(x_2) \end{aligned} \tag{A.3}$$

$$\begin{aligned} C_{t+1}^{f,(2)} &= \sigma_{t+1}(x_2) = E(\varepsilon_{t+1}(x_2) - \varepsilon_t^p(x_2)) = E(\mathbf{B}^f(x_2, y)\mathbf{d}_{e,t+1} + \overline{G}_r^{(1)}(x_2)\overline{\overline{u}}_{t+1}(x_1) + \overline{G}_r^{(2)}(x_2)\overline{\overline{u}}_{t+1}(x_2) - \varepsilon_t^p(x_2)) \\ &= \sigma_{t+1}^{trial}(x_2) + E\overline{G}_r^{(1)}(x_2)\Delta\overline{\overline{u}}(x_1) + E\overline{G}_r^{(2)}(x_2)\Delta\overline{\overline{u}}(x_2) = \sigma_{t+1}^{trial}(x_2) + E\overline{G}_r^{(1)}(x_2)\Delta\overline{\overline{\gamma}}(x_1)s(x_1) + E\overline{G}_r^{(2)}(x_2)\Delta\overline{\overline{\gamma}}(x_2)s(x_2) \end{aligned} \tag{A.4}$$

The Lagrange multipliers obtained in (106) are calculated as:

$$\begin{aligned} &\begin{bmatrix} \overline{\overline{\phi}}_{t+1}(x_1) \\ \overline{\overline{\phi}}_{t+1}(x_2) \end{bmatrix} = \begin{bmatrix} |\sigma_{t+1}(x_1)| \\ |\sigma_{t+1}(x_2)| \end{bmatrix} - \begin{bmatrix} \sigma_u - \overline{\overline{q}}_{t+1}(x_1) \\ \sigma_u - \overline{\overline{q}}_{t+1}(x_2) \end{bmatrix} \\ \Leftrightarrow &\begin{bmatrix} 0 \\ 0 \end{bmatrix} = \begin{bmatrix} \sigma_{t+1}^{trial}(x_1)s(x_1) \\ \sigma_{t+1}^{trial}(x_2)s(x_2) \end{bmatrix} + \begin{bmatrix} E\overline{G}_r^{(1)}(x_1) & E\overline{G}_r^{(2)}(x_1)s(x_2)s(x_1) \\ E\overline{G}_r^{(1)}(x_2)s(x_1)s(x_2) & E\overline{G}_r^{(2)}(x_2) \end{bmatrix} \begin{bmatrix} \Delta\overline{\overline{\gamma}}(x_1) \\ \Delta\overline{\overline{\gamma}}(x_2) \end{bmatrix} - \begin{bmatrix} \sigma_u - \overline{\overline{q}}_t(x_1) \\ \sigma_u - \overline{\overline{q}}_t(x_2) \end{bmatrix} - \begin{bmatrix} S\Delta\overline{\overline{\gamma}}(x_1) \\ S\Delta\overline{\overline{\gamma}}(x_2) \end{bmatrix} \\ \Leftrightarrow &\begin{bmatrix} 0 \\ 0 \end{bmatrix} = \begin{bmatrix} \sigma_{t+1}^{trial}(x_1)s(x_1) \\ \sigma_{t+1}^{trial}(x_2)s(x_2) \end{bmatrix} - \begin{bmatrix} \sigma_u - \overline{\overline{q}}_t(x_1) \\ \sigma_u - \overline{\overline{q}}_t(x_2) \end{bmatrix} + \begin{bmatrix} E\overline{G}_r^{(1)}(x_1) - S & E\overline{G}_r^{(2)}(x_1)s(x_2)s(x_1) \\ E\overline{G}_r^{(1)}(x_2)s(x_1)s(x_2) & E\overline{G}_r^{(2)}(x_2) - S \end{bmatrix} \begin{bmatrix} \Delta\overline{\overline{\gamma}}(x_1) \\ \Delta\overline{\overline{\gamma}}(x_2) \end{bmatrix} \\ \Leftrightarrow &\begin{bmatrix} 0 \\ 0 \end{bmatrix} = \begin{bmatrix} \overline{\overline{\phi}}_{t+1}^{trial}(x_1) \\ \overline{\overline{\phi}}_{t+1}^{trial}(x_2) \end{bmatrix} + \begin{bmatrix} E\overline{G}_r^{(1)}(x_1) - S & E\overline{G}_r^{(2)}(x_1)s(x_2)s(x_1) \\ E\overline{G}_r^{(1)}(x_2)s(x_1)s(x_2) & E\overline{G}_r^{(2)}(x_2) - S \end{bmatrix} \begin{bmatrix} \Delta\overline{\overline{\gamma}}(x_1) \\ \Delta\overline{\overline{\gamma}}(x_2) \end{bmatrix} \end{aligned} \tag{A.5}$$

A.2. Complete failure at two discontinuities

When the two discontinuities are fully open, there is no stress transfer and therefore the stresses are zero:

$$\begin{bmatrix}\sigma_{t+1}(x_1)\\ \sigma_{t+1}(x_2)\end{bmatrix} = \begin{bmatrix}0\\0\end{bmatrix}$$
$$\Leftrightarrow \begin{bmatrix}\sigma_{t+1}^{trial}(x_1)\\ \sigma_{t+1}^{trial}(x_2)\end{bmatrix} + \begin{bmatrix}E\overline{G}_r^{(1)}(x_1)s(x_1) & E\overline{G}_r^{(2)}(x_1)s(x_2)\\ E\overline{G}_r^{(1)}(x_2)s(x_1) & E\overline{G}_r^{(2)}(x_2)s(x_2)\end{bmatrix}\begin{bmatrix}\Delta\overline{\gamma}(x_1)\\ \Delta\overline{\gamma}(x_2)\end{bmatrix} = \begin{bmatrix}0\\0\end{bmatrix} \tag{A.6}$$

From this system, one can easily deduce the two Lagrange multipliers (107).

A.3. Complete failure at a single discontinuity level

Developing the system of Eq. (108) gives:

$$\begin{bmatrix}0\\0\end{bmatrix} = \begin{bmatrix}\sigma_{t+1}^{trial}(x_1)\\ \overline{\phi}_{t+1}^{trial}(x_2)\end{bmatrix} + \begin{bmatrix}E\overline{G}_r^{(1)}(x_1)s(x_1) & E\overline{G}_r^{(2)}(x_1)s(x_2)\\ E\overline{G}_r^{(1)}(x_2)s(x_1)s(x_2) & E\overline{G}_r^{(2)}(x_2) - S\end{bmatrix}\begin{bmatrix}\Delta\overline{\gamma}(x_1)\\ \Delta\overline{\gamma}(x_2)\end{bmatrix} \tag{A.7}$$

Appendix B. Integration of the cohesive model with a continuous damage model

The trial damage stresses are:

$$\begin{aligned}C_{t+1}^{f,(1),trial} &= \sigma_{t+1}^{trial}(x_1) = \overline{D}_t^{-1}(x_1)\varepsilon_{t+1}^{trial}(x_1) = \overline{D}_t^{-1}(x_1)(\mathbf{B}^f(x_1,y)\mathbf{d}_{e,t+1} + \overline{G}_r^{(1)}(x_1)\overline{u}_{t+1}^{trial}(x_1) + \overline{G}_r^{(2)}(x_1)\overline{u}_{t+1}^{trial}(x_2))\\ &= \overline{D}_t^{-1}(x_1)(\mathbf{B}^f(x_1,y)\mathbf{d}_{e,t+1} + \overline{G}_r^{(1)}(x_1)\overline{D}_t(x_1)\sigma_{t+1}^{trial}(x_1) + \overline{G}_r^{(2)}(x_1)\overline{D}_t(x_2)\sigma_{t+1}^{trial}(x_2))\end{aligned} \tag{B.1}$$

This equation can be reformulated as follows:

$$(\overline{D}_t^{-1}(x_1)\overline{G}_r^{(1)}(x_1)\overline{D}_t(x_1) - 1)\sigma_{t+1}^{trial}(x_1) + (\overline{D}_t^{-1}(x_1)\overline{G}_r^{(2)}(x_1)\overline{D}_t(x_2))\sigma_{t+1}^{trial}(x_2) = -\overline{D}_t^{-1}(x_1)\mathbf{B}^f(x_1,y)\mathbf{d}_{e,t+1} \tag{B.2}$$

The same procedure is applied for the other integration point. As in (B.1) the expression of $C_{t+1}^{f,(2),trial}$ is calculated and we obtain:

$$(\overline{D}_t^{-1}(x_2)\overline{G}_r^{(1)}(x_2)\overline{D}_t(x_1))\sigma_{t+1}^{trial}(x_1) + (\overline{D}_t^{-1}(x_2)\overline{G}_r^{(2)}(x_2)\overline{D}_t(x_2) - 1)\sigma_{t+1}^{trial}(x_2) = -\overline{D}_t^{-1}(x_2)\mathbf{B}^f(x_2,y)\mathbf{d}_{e,t+1} \tag{B.3}$$

Eqs. (B.2) and (B.3) can be written as:

$$\begin{bmatrix}\overline{D}_t^{-1}(x_1)\overline{G}_r^{(1)}(x_1)\overline{D}_t(x_1) - 1 & \overline{D}_t^{-1}(x_1)\overline{G}_r^{(2)}(x_1)\overline{D}_t(x_2)\\ \overline{D}_t^{-1}(x_2)\overline{G}_r^{(1)}(x_2)\overline{D}_t(x_1) & \overline{D}_t^{-1}(x_2)\overline{G}_r^{(2)}(x_2)\overline{D}_t(x_2) - 1\end{bmatrix}\begin{bmatrix}\sigma_{t+1}^{trial}(x_1)\\ \sigma_{t+1}^{trial}(x_2)\end{bmatrix} = \begin{bmatrix}-\overline{D}_t^{-1}(x_1)\mathbf{B}^f(x_1,y)\mathbf{d}_{e,t+1}\\ -\overline{D}_t^{-1}(x_2)\mathbf{B}^f(x_2,y)\mathbf{d}_{e,t+1}\end{bmatrix} \tag{B.4}$$

The elastic stress trial values are deduced as in (111).

B.1. Two active discontinuities per fiber

For the case of both discontinuities active per fiber, the new values of the damage cohesive stresses (114) are:

$$\begin{aligned}\sigma_{t+1}(x_1) &= \overline{D}_t^{-1}(x_1)\varepsilon_{t+1}(x_1) = \overline{D}_t^{-1}(x_1)(\mathbf{B}^f(x_1,y)\mathbf{d}_{e,t+1} + \overline{G}_r^{(1)}(x_1)\overline{u}_{t+1}(x_1) + \overline{G}_r^{(2)}(x_1)\overline{u}_{t+1}(x_2))\\ &= \overline{D}_t^{-1}(x_1)(\mathbf{B}^f(x_1,y)\mathbf{d}_{e,t+1} + \overline{G}_r^{(1)}(x_1)[\overline{D}_t(x_1)\sigma_t(x_1) + \Delta\overline{\gamma}(x_1)]s(x_1) + \overline{G}_r^{(2)}(x_1)[\overline{D}_t(x_2)\sigma_t(x_2) + \Delta\overline{\gamma}(x_2)]s(x_2))\end{aligned} \tag{B.5}$$

$$\begin{aligned}\sigma_{t+1}(x_2) &= \overline{D}_t^{-1}(x_2)\varepsilon_{t+1}(x_2) = \overline{D}_t^{-1}(x_2)(\mathbf{B}^f(x_2,y)\mathbf{d}_{e,t+1} + \overline{G}_r^{(1)}(x_2)\overline{u}_{t+1}(x_1) + \overline{G}_r^{(2)}(x_2)\overline{u}_{t+1}(x_2))\\ &= \overline{D}_t^{-1}(x_2)(\mathbf{B}^f(x_2,y)\mathbf{d}_{e,t+1} + \overline{G}_r^{(1)}(x_2)[\overline{D}_t(x_1)\sigma_t(x_1) + \Delta\overline{\gamma}(x_1)]s(x_1) + \overline{G}_r^{(2)}(x_2)[\overline{D}_t(x_2)\sigma_t(x_2) + \Delta\overline{\gamma}(x_2)]s(x_2))\end{aligned} \tag{B.6}$$

B.1.1. Calculation of the Lagrange multipliers

The calculation of the Lagrange multipliers $\Delta\overline{\gamma}(x_1)$ and $\Delta\overline{\gamma}(x_2)$ can be done using (114) and (115):

$$\begin{bmatrix}\overline{D}_t^{-1}(x_1)\mathbf{B}^f(x_1,y)\mathbf{d}_{e,t+1}s(x_1)\\ \overline{D}_t^{-1}(x_2)\mathbf{B}^f(x_2,y)\mathbf{d}_{e,t+1}s(x_2)\end{bmatrix} + \begin{bmatrix}\overline{D}_t^{-1}(x_1)\overline{G}_r^{(1)}(x_1)\overline{D}_t(x_1) & \overline{D}_t^{-1}(x_1)\overline{G}_r^{(2)}(x_1)\overline{D}_t(x_2)s(x_2)s(x_1)\\ \overline{D}_t^{-1}(x_2)\overline{G}_r^{(1)}(x_2)\overline{D}_t(x_1)s(x_1)s(x_2) & \overline{D}_t^{-1}(x_2)\overline{G}_r^{(2)}(x_2)\overline{D}_t(x_2)\end{bmatrix}\begin{bmatrix}\sigma_t(x_1)\\ \sigma_t(x_2)\end{bmatrix}$$
$$+ \begin{bmatrix}\overline{D}_t^{-1}(x_1)\overline{G}_r^{(1)}(x_1) & \overline{D}_t^{-1}(x_1)\overline{G}_r^{(2)}(x_1)s(x_2)s(x_1)\\ \overline{D}_t^{-1}(x_2)\overline{G}_r^{(1)}(x_2)s(x_1)s(x_2) & \overline{D}_t^{-1}(x_2)\overline{G}_r^{(2)}(x_2)\end{bmatrix}\begin{bmatrix}\Delta\overline{\gamma}(x_1)\\ \Delta\overline{\gamma}(x_2)\end{bmatrix} - \begin{bmatrix}\sigma_u - \overline{q}_t(x_1)\\ \sigma_u - \overline{q}_t(x_2)\end{bmatrix} - \begin{bmatrix}S\Delta\overline{\gamma}(x_1)\\ S\Delta\overline{\gamma}(x_2)\end{bmatrix} = \begin{bmatrix}0\\0\end{bmatrix}$$

Furthermore, since we have:

$$\sigma_u - \overline{\overline{q}}_t(x_1) = \sigma_t(x_1)$$
$$\sigma_u - \overline{\overline{q}}_t(x_2) = \sigma_t(x_2) \tag{B.7}$$

The use of this notation in the failure surfaces equations results:

$$\begin{bmatrix} \overline{D}_t^{-1}(x_1)\mathbf{B}^f(x_1, y)\mathbf{d}_{e,t+1}s(x_1) \\ \overline{D}_t^{-1}(x_2)\mathbf{B}^f(x_2, y)\mathbf{d}_{e,t+1}s(x_2) \end{bmatrix} + \begin{bmatrix} \overline{D}_t^{-1}(x_1)\overline{G}_r^{(1)}(x_1)\overline{\overline{D}}_t(x_1) - 1 & \overline{D}_t^{-1}(x_1)\overline{G}_r^{(2)}(x_1)\overline{\overline{D}}_t(x_2)s(x_2)s(x_1) \\ \overline{D}_t^{-1}(x_2)\overline{G}_r^{(1)}(x_2)\overline{\overline{D}}_t(x_1)s(x_1)s(x_2) & \overline{D}_t^{-1}(x_2)\overline{G}_r^{(2)}(x_2)\overline{\overline{D}}_t(x_2) - 1 \end{bmatrix} \begin{bmatrix} \sigma_t(x_1) \\ \sigma_t(x_2) \end{bmatrix}$$
$$+ \begin{bmatrix} \overline{D}_t^{-1}(x_1)\overline{G}_r^{(1)}(x_1) - S & \overline{D}_t^{-1}(x_1)\overline{G}_r^{(2)}(x_1)s(x_2)s(x_1) \\ \overline{D}_t^{-1}(x_2)\overline{G}_r^{(1)}(x_2)s(x_1)s(x_2) & \overline{D}_t^{-1}(x_2)\overline{G}_r^{(2)}(x_2) - S \end{bmatrix} \begin{bmatrix} \Delta\overline{\overline{y}}(x_1) \\ \Delta\overline{\overline{y}}(x_2) \end{bmatrix} = \begin{bmatrix} 0 \\ 0 \end{bmatrix}$$

The latter equation is reformulated as follows:

$$\begin{bmatrix} \overline{D}_t^{-1}(x_1)\overline{G}_r^{(1)}(x_1)\overline{\overline{D}}_t(x_1) - 1 & \overline{D}_t^{-1}(x_1)\overline{G}_r^{(2)}(x_1)\overline{\overline{D}}_t(x_2)s(x_2)s(x_1) \\ \overline{D}_t^{-1}(x_2)\overline{G}_r^{(1)}(x_2)\overline{\overline{D}}_t(x_1)s(x_1)s(x_2) & \overline{D}_t^{-1}(x_2)\overline{G}_r^{(2)}(x_2)\overline{\overline{D}}_t(x_2) - 1 \end{bmatrix}^{-1} \begin{bmatrix} \overline{D}_t^{-1}(x_1)\mathbf{B}^f(x_1, y)\mathbf{d}_{e,t+1}s(x_1) \\ \overline{D}_t^{-1}(x_2)\mathbf{B}^f(x_2, y)\mathbf{d}_{e,t+1}s(x_2) \end{bmatrix} + \begin{bmatrix} \sigma_t(x_1) \\ \sigma_t(x_2) \end{bmatrix}$$
$$+ \begin{bmatrix} \overline{D}_t^{-1}(x_1)\overline{G}_r^{(1)}(x_1)\overline{\overline{D}}_t(x_1) - 1 & \overline{D}_t^{-1}(x_1)\overline{G}_r^{(2)}(x_1)\overline{\overline{D}}_t(x_2)s(x_2)s(x_1) \\ \overline{D}_t^{-1}(x_2)\overline{G}_r^{(1)}(x_2)\overline{\overline{D}}_t(x_1)s(x_1)s(x_2) & \overline{D}_t^{-1}(x_2)\overline{G}_r^{(2)}(x_2)\overline{\overline{D}}_t(x_2) - 1 \end{bmatrix}^{-1} \begin{bmatrix} \overline{D}_t^{-1}(x_1)\overline{G}_r^{(1)}(x_1) - S & \overline{D}_t^{-1}(x_1)\overline{G}_r^{(2)}(x_1)s(x_2)s(x_1) \\ \overline{D}_t^{-1}(x_2)\overline{G}_r^{(1)}(x_2)s(x_1)s(x_2) & \overline{D}_t^{-1}(x_2)\overline{G}_r^{(2)}(x_2) - S \end{bmatrix}$$
$$\begin{bmatrix} \Delta\overline{\overline{y}}(x_1) \\ \Delta\overline{\overline{y}}(x_2) \end{bmatrix} = \begin{bmatrix} 0 \\ 0 \end{bmatrix} \tag{B.8}$$

From Eq. (B.8) it can be noted that the first two terms are the expressions of the failure surface ($\overline{\overline{\phi}}_{t+1}^{trial}(x_1)$ and $\overline{\overline{\phi}}_{t+1}^{trial}(x_1)$) derived from the elastic prediction multiplied by a factor of (-1). This makes possible to get a simpler expression:

$$\begin{bmatrix} \overline{\overline{\phi}}_{t+1}^{trial}(x_1) \\ \overline{\overline{\phi}}_{t+1}^{trial}(x_2) \end{bmatrix} = \begin{bmatrix} \overline{D}_t^{-1}(x_1)\overline{G}_r^{(1)}(x_1)\overline{\overline{D}}_t(x_1) - 1 & \overline{D}_t^{-1}(x_1)\overline{G}_r^{(2)}(x_1)\overline{\overline{D}}_t(x_2)s(x_2)s(x_1) \\ \overline{D}_t^{-1}(x_2)\overline{G}_r^{(1)}(x_2)\overline{\overline{D}}_t(x_1)s(x_1)s(x_2) & \overline{D}_t^{-1}(x_2)\overline{G}_r^{(2)}(x_2)\overline{\overline{D}}_t(x_2) - 1 \end{bmatrix}^{-1}$$
$$\times \begin{bmatrix} \overline{D}_t^{-1}(x_1)\overline{G}_r^{(1)}(x_1) - S & \overline{D}_t^{-1}(x_1)\overline{G}_r^{(2)}(x_1)s(x_2)s(x_1) \\ \overline{D}_t^{-1}(x_2)\overline{G}_r^{(1)}(x_2)s(x_1)s(x_2) & \overline{D}_t^{-1}(x_2)\overline{G}_r^{(2)}(x_2) - S \end{bmatrix} \begin{bmatrix} \Delta\overline{\overline{y}}(x_1) \\ \Delta\overline{\overline{y}}(x_2) \end{bmatrix}$$

The Lagrange multipliers are obtained as in (116).

B.2. Complete failure at two discontinuities

The system of Eq. (117) gives:

$$\begin{bmatrix} \overline{D}_t^{-1}(x_1)\mathbf{B}^f(x_1, y)\mathbf{d}_{e,t+1} \\ \overline{D}_t^{-1}(x_2)\mathbf{B}^f(x_2, y)\mathbf{d}_{e,t+1} \end{bmatrix} + \begin{bmatrix} \overline{D}_t^{-1}(x_1)\overline{G}_r^{(1)}(x_1)\overline{\overline{D}}_t(x_1)s(x_1) & \overline{D}_t^{-1}(x_1)\overline{G}_r^{(2)}(x_1)\overline{\overline{D}}_t(x_2)s(x_2) \\ \overline{D}_t^{-1}(x_2)\overline{G}_r^{(1)}(x_2)\overline{\overline{D}}_t(x_1)s(x_1) & \overline{D}_t^{-1}(x_2)\overline{G}_r^{(2)}(x_2)\overline{\overline{D}}_t(x_2)s(x_2) \end{bmatrix} \begin{bmatrix} \sigma_t(x_1) \\ \sigma_t(x_2) \end{bmatrix}$$
$$+ \begin{bmatrix} \overline{D}_t^{-1}(x_1)\overline{G}_r^{(1)}(x_1)s(x_1) & \overline{D}_t^{-1}(x_1)\overline{G}_r^{(2)}(x_1)s(x_2) \\ \overline{D}_t^{-1}(x_2)\overline{G}_r^{(1)}(x_2)s(x_1) & \overline{D}_t^{-1}(x_2)\overline{G}_r^{(2)}(x_2)s(x_2) \end{bmatrix} \begin{bmatrix} \Delta\overline{\overline{y}}(x_1) \\ \Delta\overline{\overline{y}}(x_2) \end{bmatrix} = \begin{bmatrix} 0 \\ 0 \end{bmatrix}$$

Therefore, the system (118) is deduced.

B.3. Complete failure at a single discontinuity level

The development of the first equation of the system (119) gives:

$$\overline{D}_t^{-1}(x_1)\mathbf{B}^f\left(x_1, y\right)\mathbf{d}_{e,t+1} + [\overline{D}_t^{-1}(x_1)\overline{G}_r^{(1)}(x_1)\overline{\overline{D}}_t(x_1)s(x_1) \quad \overline{D}_t^{-1}(x_1)\overline{G}_r^{(2)}(x_1)\overline{\overline{D}}_t(x_2)s(x_2)] \begin{bmatrix} \sigma_t(x_1) \\ \sigma_t(x_2) \end{bmatrix}$$
$$+ [\overline{D}_t^{-1}(x_1)\overline{G}_r^{(1)}(x_1)s(x_1) \quad \overline{D}_t^{-1}(x_1)\overline{G}_r^{(2)}(x_1)s(x_2)] \begin{bmatrix} \Delta\overline{\overline{y}}(x_1) \\ \Delta\overline{\overline{y}}(x_2) \end{bmatrix} = 0 \tag{B.9}$$

The second equation of the system (119) becomes:

$$\overline{D}_t^{-1}(x_2)\mathbf{B}^f\left(x_1, y\right)\mathbf{d}_{e,t+1}s(x_2) + [\overline{D}_t^{-1}(x_2)\overline{G}_r^{(1)}(x_2)\overline{\overline{D}}_t(x_1)s(x_1)s(x_2) \quad \overline{D}_t^{-1}(x_2)\overline{G}_r^{(2)}(x_2)\overline{\overline{D}}_t(x_2) - 1] \begin{bmatrix} \sigma_t(x_1) \\ \sigma_t(x_2) \end{bmatrix}$$
$$+ [\overline{D}_t^{-1}(x_2)\overline{G}_r^{(1)}(x_2)s(x_1)s(x_2) \quad \overline{D}_t^{-1}(x_2)\overline{G}_r^{(2)}(x_2) - S] \begin{bmatrix} \Delta\overline{\overline{y}}(x_1) \\ \Delta\overline{\overline{y}}(x_2) \end{bmatrix} = 0 \tag{B.10}$$

The two equations developed above are written as:

$$\begin{bmatrix} \overline{D}_t^{-1}(x_1)\mathbf{B}^f(x_1,y)\mathbf{d}_{e,t+1} \\ \overline{D}_t^{-1}(x_2)\mathbf{B}^f(x_2,y)\mathbf{d}_{e,t+1}s(x_2) \end{bmatrix} + \begin{bmatrix} \overline{D}_t^{-1}(x_1)\overline{G}_r^{(1)}(x_1)\overline{\overline{D}}_t(x_1)s(x_1) & \overline{D}_t^{-1}(x_1)\overline{G}_r^{(2)}(x_1)\overline{\overline{D}}_t(x_2)s(x_2) \\ \overline{D}_t^{-1}(x_2)\overline{G}_r^{(1)}(x_2)\overline{\overline{D}}_t(x_1)s(x_1)s(x_2) & \overline{D}_t^{-1}(x_2)\overline{G}_r^{(2)}(x_2)\overline{\overline{D}}_t(x_2) - 1 \end{bmatrix} \begin{bmatrix} \sigma_t(x_1) \\ \sigma_t(x_2) \end{bmatrix}$$
$$+ \begin{bmatrix} \overline{D}_t^{-1}(x_1)\overline{G}_r^{(1)}(x_1)s(x_1) & \overline{D}_t^{-1}(x_1)\overline{G}_r^{(2)}(x_1)s(x_2) \\ \overline{D}_t^{-1}(x_2)\overline{G}_r^{(1)}(x_2)s(x_1)s(x_2) & \overline{D}_t^{-1}(x_2)\overline{G}_r^{(2)}(x_2) - S \end{bmatrix} \begin{bmatrix} \Delta\overline{\overline{\gamma}}(x_1) \\ \Delta\overline{\overline{\gamma}}(x_2) \end{bmatrix} = \begin{bmatrix} 0 \\ 0 \end{bmatrix} \tag{B.11}$$

The Lagrange multipliers are finally deduced as in (120).

References

[1] Chan EC-Y. Nonlinear geometric material and time dependent analysis of reinforced concrete shells with edge beams [Ph.D. thesis]. Berkeley: University of California; 1983.
[2] Scordelis AC. Computer models for nonlinear analysis of reinforced and prestressed concrete structures. PCI J 1984;29(6):116–35.
[3] Izzuddin BA. Nonlinear dynamic analysis of framed structures [Ph.D. thesis]. Imperial College London (University of London); 1990.
[4] Spacone E, Filippou FC, Taucer FF. Fibre beam-column model for non-linear analysis of R/C frames: part I. formulation. Earthquake Eng Struct Dynam 1996;25(7):711–26.
[5] Kotronis P, Mazars J. Simplified modelling strategies to simulate the dynamic behaviour of {R}/{C} walls. J Earthquake Eng 2005;9(2):285–306.
[6] Kotronis P, Ragueneau F, Mazars J. A simplified modelling strategy for R/C walls satisfying PS92 and EC8 design. Eng Struct 2005;27(8):1197–208. https://doi.org/10.1016/j.engstruct.2005.03.003. URL <http://linkinghub.elsevier.com/retrieve/pii/S0141029605001136>.
[7] Ile N, Nguyen X-H, Kotronis P, Mazars J, Reynouard JM. Shaking table tests of lightly {RC} walls: numerical simulations. J Earthquake Eng 2008;12(6):849–978.
[8] Grange S, Kotronis P, Mazars J. Numerical modelling of the seismic behaviour of a 7-story building: NEES benchmark. Mater Struct 2008;42(10):1433–42. https://doi.org/10.1617/s11527-008-9462-y. URL <http://www.springerlink.com/index/10.1617/s11527-008-9462-y>.
[9] Grange S, Botrugno L, Kotronis P, Tamagnini C. The effects of Soil-Structure Interaction on a reinforced concrete viaduct. Earthquake Eng Struct Dynam 2011;41(11):1549–68. https://doi.org/10.1002/eqe. URL <http://onlinelibrary.wiley.com/doi/10.1002/eqe.2230/full>.
[10] Desprez C, Mazars J, Kotronis P, Paultre P. Damage model for FRP-confined concrete columns under cyclic loading. Eng Struct 2013;48:519–31. https://doi.org/10.1016/j.engstruct.2012.09.019. URL <http://linkinghub.elsevier.com/retrieve/pii/S014102961200497X>.
[11] Desprez C, Kotronis P, Mazars J. Seismic vulnerability assessment of a RC structure before and after FRP retrofitting. Bull Earthq Eng 2015;13:539–64. https://doi.org/10.1007/s10518-014-9621-1. URL <http://link.springer.com/10.1007/s10518-014-9621-1>.
[12] Mazars J, Kotronis P, Ragueneau F, Casaux G. Using multifiber beams to account for shear and torsion. Comput Methods Appl Mech Eng 2006;195(52):7264–81. https://doi.org/10.1016/j.cma.2005.05.053. URL <http://linkinghub.elsevier.com/retrieve/pii/S0045782505004123>.
[13] Feng DC, Xu J. An efficient fiber beam-column element considering flexure-shear interaction and anchorage bond-slip effect for cyclic analysis of RC structures. Bull Earthq Eng 2018:1–28.
[14] Spacone E, Limkatanyu S. Response of RC members including bond-slip effects. ACI Struct J 2000;6:831–9.
[15] Pinho R, Elnashai A. Dynamic collapse testing of a full-scale four storey RC frame. ISET J Earthquake Technol 2000;37(4):143–63.
[16] Ranzo G, Petrangeli M. A fibre finite beam element with section shear modelling for seismic analysis of RC structures. J Earthquake Eng 1988;2(03):443–7.
[17] Petrangeli M, Pinto PE, Ciampi V. Fiber element for cyclic bending and shear of RC structures. I: theory. J Eng Mech 1999;125(9):994–1001.
[18] Marini A, Spacone E. Analysis of reinforced concrete elements including shear effects. ACI Struct J 2006;103(5):645.
[19] Bairan Garcia JM, Mari Bernat AR. Coupled model for the non-linear analysis of anisotropic sections subjected to general 3D loading. Part 1: theoretical formulation. Comput Struct 2006;84(31–32):2254–63. https://doi.org/10.1016/j.compstruc.2006.08.036.
[20] Navarro Gregori J, Miguel Sosa P, Fernandez Prada MA, Filippou FC. A 3D numerical model for reinforced and prestressed concrete elements subjected to combined axial, bending, shear and torsion loading. Eng Struct 2007;29(12):3404–19.
[21] Šćulac P, Jelenić G, Škec L. Kinematics of layered reinforced-concrete planar beam finite elements with embedded transversal cracking. Int J Solids Struct 2014;51(1):74–92. https://doi.org/10.1016/j.ijsolstr.2013.09.011. URL <http://linkinghub.elsevier.com/retrieve/pii/S0020768313003661>.
[22] Jukić M, Brank B, Ibrahimbegović A. Failure analysis of reinforced concrete frames by beam finite element that combines damage, plasticity and embedded discontinuity. Eng Struct 2014;75:507–27. https://doi.org/10.1016/j.engstruct.2014.06.017. URL <http://linkinghub.elsevier.com/retrieve/pii/S0141029614003733>.
[23] Caillerie D, Kotronis P, Cybulski R. A Timoshenko finite element straight beam with internal degrees of freedom. Int J Numer Anal Meth Geomech 2015;39(16):1753–73. https://doi.org/10.1002/nag.
[24] Ian DM, Doherty IW, Court DM, Armstrong CG. Coupling 1d beams to 3d bodies. Proc. 7 th int. meshing roundtable. Sandia National Laboratories; 1998. p. 285–93.
[25] Giry C. Modélisation objective de la localisation des déformations et de la fissuration dans les structures en béton armé [Ph.D. thesis]. Université de Grenoble; 2011.
[26] Capdevielle S, Grange S, Dufour F, Desprez C. A multifiber beam model coupling torsional warping and damage for reinforced concrete structures. Eur J Environ Civ Eng 2016;20(8):914–35. https://doi.org/10.1080/19648189.2015.1084384. URL <http://www.tandfonline.com/doi/full/10.1080/19648189.2015.1084384>.
[27] Khoder N, Grange S, Sieffert Y. Enhancement of a two-dimensional multifibre beam element in the case of reinforced concrete structures for taking into account the lateral confinement of concrete due to stirrups. Eur J Environ Civ Eng 2018;0(0):0. https://doi.org/10.1080/19648189.2018.1446364. (online).
[28] Armero F, Ehrlich D. An analysis of strain localization and wave propagation in plastic models of beams at failure. Comput Methods Appl Mech Eng 2004;193(30–32):3129–71. https://doi.org/10.1016/j.cma.2003.07.015.
[29] Ehrlich D, Armero F. Finite element methods for the analysis of softening plastic hinges in beams and frames. Comput Mech 2005;35(4):237–64. https://doi.org/10.1007/s00466-004-0575-z.
[30] Armero F, Ehrlich D. Numerical modeling of softening hinges in thin Euler-Bernoulli beams. Comput Struct 2006;84(10–11):641–56. https://doi.org/10.1016/j.compstruc.2005.11.010.
[31] Dujc J, Brank B, Ibrahimbegović A. Multi-scale computational model for failure analysis of metal frames that includes softening and local buckling. Comput Methods Appl Mech Eng 2010;199(21–22):1371–85. https://doi.org/10.1016/j.cma.2009.09.003.
[32] Pham BH, Davenne L, Brancherie D, Ibrahimbegović A. Stress resultant model for ultimate load design of reinforced-concrete frames: combined axial force and bending moment. Comput Concr 2010;7(4):303–15. https://doi.org/10.12989/cac.2010.7.4.303. URL <http://koreascience.or.kr/journal/view.jsp?kj=KJKHDQ&py=2010&vnc=v7n4&sp=303>.
[33] Jukić M, Brank B, Ibrahimbegović A. Embedded discontinuity finite element formulation for failure analysis of planar reinforced concrete beams and frames. Eng Struct 2012;50:115–25. https://doi.org/10.1016/j.engstruct.2012.07.028.
[34] Bui NN, Ngo VM, Nikolic M, Brancherie D, Ibrahimbegović A. Enriched Timoshenko beam finite element for modeling bending and shear failure of reinforced concrete frames. Comput Struct 2014;143:9–18. https://doi.org/10.1016/j.compstruc.2014.06.004. URL <http://linkinghub.elsevier.com/retrieve/pii/S0045794914001369>.
[35] Nikolic M, Ibrahimbegovic A, Miscevic P. Brittle and ductile failure of rocks: embedded discontinuity approach for representing mode i and mode ii failure

mechanisms. Int J Numer Methods Eng 2015;102(8):1507–26.
[36] Nikolic M, Ibrahimbegovic A, Miscevic P. Discrete element model for the analysis of fluid-saturated fractured poro-plastic medium based on sharp crack representation with embedded strong discontinuities. Comput Methods Appl Mech Eng 2016;298:407–27.
[37] Bitar I, Kotronis P, Benkemoun N, Grange S. A generalized timoshenko beam with embedded rotation discontinuity. Finite Elem Anal Des 2018;150:34–50. https://doi.org/10.1016/j.finel.2018.07.002. URL <http://www.sciencedirect.com/science/article/pii/S0168874X18301999>.
[38] Pham BH, Brancherie D, Davenne L, Ibrahimbegović A. Stress-resultant models for ultimate load design of reinforced concrete frames and multi-scale parameter estimates. Comput Mech 2012;51(3):347–60. https://doi.org/10.1007/s00466-012-0734-6. URL <http://link.springer.com/10.1007/s00466-012-0734-6>.
[39] Pegon P. A Timoshenko simple beam element in Castem 2000. Special publication Nr. I.94.04. Applied Mechanics Unit, Institute for Safety Technology, Joint Research Centre, Commission of the European Communities, I-21020 ISPRA (VA), Italy; 1994.
[40] Guedes J, Pegon P, Pinto AV. A Fibre/Timoshenko beam element in Castem 2000. Special publication Nr. I.94.31. Applied Mechanics Unit, Institute for Safety Technology, Joint Research Centre, Commission of the European Communities, I-21020 ISPRA (VA), Italy; 1994.
[41] Friedman Z, Kosmatka JB. An improved two-node Timoshenko beam Finite Element. Comput Struct 1993;47(3):473–81.
[42] Bitar I, Grange S, Kotronis P, Benkemoun N. A comparison of displacement-based timoshenko multi-fiber beams finite element formulations and elasto-plastic applications. Eur J Environ Civ Eng 2018;22(4):464–90. https://doi.org/10.1080/19648189.2016.1210031.
[43] Zienkiewicz OC, Taylor RL. Finite element method – the basis. Oxford: Butterworth-heinemann; 2000.
[44] Bitar I. Modeling the failure of reinforced concrete structures using generalized and multifiber finite element beams [Ph.D. thesis]. Ecole Centrale de Nantes; 2017.
[45] Dvorkin EN, Cuitiño AM, Gioia G. Finite elements with displacement interpolated embedded localization lines insensitive to mesh size and distortions. Int J Numer Methods Eng 1990;30(September 1989):541–64. https://doi.org/10.1002/nme.1620300311.
[46] Oliver J. Modelling strong discontinuities in solid mechanics via strain softening constitutive equations. Part 1: fundamentals. Int J Numer Methods Eng 1996;39(January):3575–600. https://doi.org/10.1002/(SICI)1097-0207(19961115)39:21<3601::AID-NME64>3.0.CO;2-4.
[47] Taylor RL, Simo JC, Zienkiewicz OC, Chan ACH. The patch test – a condition for assessing FEM convergence. Int J Numer Methods Eng 1986;22(1):39–62. https://doi.org/10.1002/nme.1620220105. URL <http://doi.wiley.com/10.1002/nme.1620220105>.
[48] Irons BM, Razzaque A. Experience with the patch test for convergence of finite elements, The mathematical foundations of the finite element method with applications to partial differential equations 557.
[49] Ibrahimbegović A. Mécanique non linéaire des solides déformables: Formulation théorique et résolution par éléments finis. Hermes Science Publ.; 2006.
[50] Mazars J. A description of micro- and macroscale damage of concrete structures. Eng Fract Mech 1986;25(5–6):729–37. https://doi.org/10.1016/0013-7944(86)90036-6.
[51] Simo JC, Ju JW. Strain- and stress-based continuum damage models-I. Formulation. Int J Solids Struct 1987;23(7):821–40. https://doi.org/10.1016/0020-7683(87)90083-7.
[52] Simo JC, Ju JW. Strain- and stress-based continuum damage models-II. Computational aspects. Int J Solids Struct 1987;23(7):841–69. https://doi.org/10.1016/0020-7683(87)90084-9.
[53] Borderie CL. Phenomènes unilateraux dans un matériau endommageable: Modélisation et application à l'analyse de structures en béton [Ph.D. thesis]. Université de Paris 06; 1991.
[54] Jirásek M. Nonlocal damage mechanics with application to concrete. Revue Française de Génie Civil 2004;8(5–6):683–707. https://doi.org/10.1080/12795119.2004.9692625.
[55] Mazars J, Hamon F, Grange S. A new 3D damage model for concrete under monotonic, cyclic and dynamic loadings. Mater Struct 2014:3779–93. https://doi.org/10.1617/s11527-014-0439-8. URL <http://link.springer.com/10.1617/s11527-014-0439-8>.
[56] Ortiz M. A constitutive theory for the inelastic behavior of concrete. Mech Mater 1985;4(1):67–93. https://doi.org/10.1016/0167-6636(85)90007-9. URL <http://www.sciencedirect.com/science/article/pii/0167663685900079>.
[57] Borja RI. Plasticity, modeling & computation. Springer; 2013.
[58] Cranston WB. Tests on reinforced concrete frames: Pinned portal frames. Tech. rep. London: Cement and Concrete Association; 1965.
[59] Saje M, Planinc I, Bratina S. Large displacements and instability of beam-like structural systems, engineering structures under extreme conditions: multi-physics and multi-scale computer models in nonlinear analysis and optimal design. Amsterdam: IOS Press; 2005. p. 329–50.
[60] Jukić M. Finite elements for modeling of localized failure in reinforced concrete [Ph.D. thesis]. École normale supérieure de Cachan; 2013.
[61] Bažant ZP, Pan J, Pijaudier-Cabot G. Softening in reinforced concrete beams and frames. J Struct Eng 1987;113(12):2333–47. https://doi.org/10.1061/(ASCE)0733-9445(1987)113:12(2333).